TÉCNICO LISBOA

Alignment Control of an Optical Link in a Turbulent Channel for Satellite Communication Systems

Ana Carolina Teixeira Borralho

Thesis to obtain the Master of Science Degree in

Electrical and Computer Engineering

Supervisor(s): Prof. Dr. Paulo Sérgio de Brito André
Prof. Dr. Manfred Niehus

Examination Committee

Chairperson: Prof. José Eduardo Charters Ribeiro da Cunha Sanguino
Supervisor: Prof. Paulo Sérgio de Brito André
Member of the Committee: Prof. António Luís Campos da Silva Topa

November 2021

Declaração

I declare that this document is an original work of my own authorship and that it fulfills all the requirements of the Code of Conduct and Good Practices of the Universidade de Lisboa.

À minha querida Didi,

Obrigada pela tua fé, força e amor incondicional.

Acknowledgments

A very remarkable and challenging chapter of my life ends with the deliver of this dissertation. Over the last six years I faced many challenges, but with the right people on my side, I managed to overcome all of them. I would like to take this opportunity to thank to everyone that somehow had a significant role in my academic journey.

To my supervisors, Professor Paulo André and Professor Manfred Niehus, for the vote of confidence, extreme availability, patience and guidance through the last year. Thank you for the opportunity of working in such an interesting area and participating in the project QSat, where I learned so much. Thank you to Instituto de Telecomunicações for allowing me to set up my experience in a laboratory and provide all the required equipment.

To my colleague and now friend, Pedro Mendes, who has been my company for the last six months in QuTe Lab. I appreciate all your help to assemble my experimental set up, but specially your company in this phase where everyone was at home and we were the only ones in the lab.

To the friends that Instituto Superior Técnico gave me: Carolina, Barroso, Cíntia, Miguel, Raul and João: with you I shared endless laboratory works, projects, reports, tests and exams. You always understood my difficulties and the feeling that I was never alone helped me to surpass the hardest and busiest weeks of our degree. I am sure the bond we created will stay with us for the rest of our lives. To Rodolfo and Pires, who accompanied me closely during my dissertation, thank you for making me laugh at every break and for giving me great examples of discipline and hard work.

To all my close friends, for always showing your support with words of motivation and hope and understanding all the times I stayed studying and doing projects instead of going out.

Finally, and most important, to my family. I remember your excitement when I was accepted to study in Instituto Superior Técnico. You followed my journey, celebrating my victories and giving me strength to keep going. To my grandparents Didi and Nene, who welcomed me into their home when I moved to Lisbon to study and gave me so much love and comfort. To my parents. This could never happen without you. I will be forever grateful for your support, patience, encouragement, care and most of all, for raising me to be an educated independent woman. I hope this achievement is the realization of the dream that we always had for me.

Resumo

A utilização de satélites nas comunicações revolucionou a transmissão de informação a longa distância, permitindo interligar pontos cada vez mais distantes. Durante muito tempo foram utilizados sistemas de radiofrequência. No entanto, o espetro rádio acabou por ficar congestionado e revela dificuldade em responder às exigências atuais de ritmo de transmissão, largura de banda, segurança e capacidade. Os sistemas óticos começaram a ser explorados e as suas múltiplas vantagens como um espetro livre de licenças, grande largura de banda disponível, alcance de altos ritmos de transmissão e requisitos de menores dimensões e peso e menor consumo de potência, fizeram com que se tornassem uma interessante alternativa para comunicações entre a Terra e o espaço.

Os sistemas óticos conseguem alta precisão através do uso de feixes laser estreitos. No entanto, quando um satélite está em órbita torna-se extremamente desafiante o alinhamento entre terminais, não só pela estreiteza dos feixes, como pela degradação do sinal causada pela propagação na atmosfera terrestre. Estes problemas são ampliados quando se trata de satélites pequenos, devido às suas limitações de tamanho, peso e potência.

O objetivo desta dissertação é estudar um sistema do apontamento em malha fechada que otimize o alinhamento entre terminais emissor e recetor de uma comunicação ótica entre um pequeno satélite em baixa órbita e a Terra, testar o sistema em condições de turbulência atmosférica e perspetivar a viabilidade de uma ligação a longa distância.

O sistema de apontamento implementado recebe o sinal de *uplink* e corrige a posição do sinal de *downlink* por forma a haver alinhamento. O controlo da posição foi feito através de um sistema de controlo proporcional, integral e derivativo em malha fechada que permite corrigir até 3.4 mrad. O sistema foi montado experimentalmente e testado sob condições de turbulência, mostrando que é possível melhorar o desempenho da ligação.

Palavras-chave: Comunicações óticas; Comunicações com satélites; Comunicação ótica em espaço livre; Apontamento, aquisição e seguimento; Controlo do alinhamento em malha fechada; Turbulência atmosférica.

Abstract

The use of satellites in communications has revolutionized the transmission of information, allowing to interconnect increasingly distant points. Radio frequency systems have been used for a long time. However, these ended up becoming congested and show difficulty in meeting the current requirements of bit rate, bandwidth, security and capacity. Optical systems began to be explored and their multiple advantages over radio systems have made them an interesting alternative for communications between Earth and space.

Optical systems achieve high accuracy by using narrow laser beams. However, when a satellite is in orbit the alignment between terminals becomes extremely challenging, not only because of the narrowness of the beams but also because of the degradation of the signal caused by the propagation in the atmosphere. These problems are magnified when we refer to small satellites, due to their size, weight and power constraints.

The objective of this dissertation is to study a closed loop pointing system that optimizes the alignment between emitter and receiver terminals of an optical communication between a small satellite in low orbit and the Earth, test the system under atmospheric turbulence conditions and perspective the feasibility of a long range link.

The implemented pointing system receives the uplink beacon and corrects the position of the downlink signal so that there is alignment. The position control was done using a closed loop proportional, integral and derivative control system that allows corrections until 3.4 mrad. The system was set up experimentally and tested under turbulent conditions, showing that is possible to improve the link performance.

Keywords: Optical communications; Satellite communications; Free space optics; Pointing, acquisition and tracking; Closed loop alignment control; Atmospheric turbulence.

Contents

List of Tables

List of Figures

List of Acronyms

ACO	Assymetrically Clipped Optical
ADCS	Attitude Determination and Control System
AO	Adaptive Optics
APD	Avalanche Photodiode
BER	Bit error rate
CLICK	CubeSat Laser Infrared CrosslinK Mission
CMOS	Complementary metal–oxide–semiconductor
CW	Continuous Wave
DC	Direct Current
DCO	Direct Current Optical
DPIM	Digital Pulse Interval Modulation
ESA	European Space Agency
ETS-VI	Engineering Test Satellite-VI
FEC	Forward Error Correction
FPS	Fine Pointing System
FSO	Free Space Optics
FSM	Fast Steering Mirror
FoV	Field of View
GEOS-II	Geodetic Earth Orbiting Satellite-II
GOPEX	Galileo Optical Experiment
GOLD	Ground/Orbiter Lasercom Demonstration
GS	Ground Station
IM/DD	Intensity Modulation/Direct Detection
ISC	Inter-satellite Communication
ISI	Intersymbol Interference
JPL	Jet Propulsion Laboratory
LDPC	Low Density Parity Check
LED	Light Emitting Diode
LEO	Low Earth Orbit
LLCD	Lunar Laser Communication Demonstration

MEMS	Micro Electro Mechanical System
MIT	Massachusetts Institute of Technology
ND	Neutral Density
NEP	Noise Equivalent Power
NICT	National Institute of Information and Communications Technology
NODE	Nanosatellite Optical Downlink Experiment
NRZ	Non-Return to Zero
OAM	Orbital Angular Momentum
OCTL	Optical Communications Telescope Laboratory
OFDM	Orthogonal Frequency Division Multiplexing
OGS	Optical Ground Station
OICETS	Optical Inter-Orbit Communications Engineering Test Satellite
OOK	On-Off Keying
OWC	Optical Wireless Communications
PAM	Pulse Amplitude Modulation
PAT	Pointing, Acquisition and Tracking
PDF	Probability Density Function
PID	Proportional Integral and Derivative
PPM	Pulse Position Modulation
QAM	Quadrature Amplitude Modulation
QKD	Quantum Key Distribution
QPKS	Quadrature Phase Shift Keying
QoS	Quality of Service
RF	Radiofrequency
RME	Relay Mirror Experiment
SILEX	Semi-conductor Inter SatelliteLink Experiment
SIM	Sub-Carreier Intensity Modulation
SOTA	Small Optical TrAnsponder
SNR	Signal-to-Noise Ratio
STAR Lab	Space, Telecommunications, Astronomy and Radiation Laboratory
SWaP	Size, Weight and Power
TBIRD	TeraByte InfraRed Delivery
TTL	Transistor-transistor-logic
UAV	Unmanned Arial Vehicle
VLC	Visible Light Communication
WDM	Wavelength Division Multiplexing

List of Symbols

λ	Wavelength
R	Responsivity
P_r	Received Power
σ_{shot}	Shot Noise Variance
$\sigma_{thermal}$	Thermal Noise Variance
S	Signal Power
N	Noise Power
R_b	Bit Rate
Δf	Bandwidth
K_B	Boltzmann Constant
T	Absolute Temperature
R	Resistance
q	Electron Charge
i_d	Photodiode Dark Current
P_n	Input Noise Power
P_{NEP}	Noise Power due to NEP
G	Amplifier Gain
P_a	Noise Power due to Amplifier
θ_{div}	Divergence Angle
P_t	Transmitted Power
γ	Attenuation Coefficient
α_{ml}	Molecular Absorption Coefficient
α_{al}	Aerosol Absorption Coefficient
β_{ml}	Molecular Scattering Coefficient
β_{al}	Aerosol Scattering Coefficient
N_p	Number of Particles per Volume Unit
A_p	Cross-sectional Area of Scattering
V	Visibility Range
q	Size Distribution Coefficient of the Scattering Particles
γ_{rain}	Attenuation due to Rain

P	Precipitation intensity
γ_{snow}	Attenuation due to Snow
S	Snowfall Rate
γ_{dust}	Attenuation due to Dust
$p(t)$	Position of the calibration laser over time
$e(t)$	Pointing error over time
K_d	Derivative Gain
K_i	Integral Gain
K_p	Proportional Gain
Θ_{FSM}	Angular Position of the FSM
$V_{driving}$	FSM Driving Voltage
ω_0	Ressonance Frequency
Q	Quality Factor

Chapter 1

Introduction

The control of the alignment of an optical link in a turbulent channel is essential to guarantee the success of a communication between a satellite and a ground station (GS), being satellite systems responsible for a global network. Section 1.1 starts with the motivation to develop a fine pointing system for a small satellite. Section 1.2 presents the state of the art, where several satellite-to-satellite and satellite-to-ground demonstrations are reported. Section 1.3 explains the objectives of the dissertation and 1.4 describes its outline.

1.1 Motivation

Communication is one of the most important activities of the humanity. The desire to communicate remotely propelled the appearance of long haul communication, which consisted of the creation of public networks with systems that cover great distances such as nationwide or worldwide. These systems started with wired connections, firstly with electrical cables and later with optical fiber. But the demand to connect increasingly distant points ended up showing that there are some situations where it is impossible or impractical to use wires [1]. This led to a particular interest in wireless communications, and as communication technologies evolved, satellites appeared and became a promising technology for long haul communication and to connect points where terrestrial systems cannot access [2].

The satellite communication started being explored using the radio frequency (RF) domain, but these systems find it difficult to meet all the requirements posed nowadays. The demand for high bit rate, bandwidth and capacity has grown significantly in recent years, leading to the congestion of RF spectrum and the search for alternatives. The growing studies in the field of optics revealed optical communications systems as a very interesting option [3].

Optical wireless communication (OWC) systems offer many advantages over RF systems such as large available bandwidth, high data rate, license free spectrum, less power comsumption and low mass requirements and high security, so it is easy to see their potential for high-speed broadband connections [4]. Outdoor OWC, better known as free space optics (FSO), allow information to be transmitted using an unguided channel, which is the case of atmospheric propagation. Furthermore, FSO makes it possible

to establish ground-to-satellite, satellite-to-ground and satellite-to-satellite links.

However, the performance of optical links is affected by many factors such as beam divergence over long distances, pointing errors, strong atmospheric attenuation and atmospheric turbulence [1]. These factors cause degradation and, in extreme cases, even loss of the link. Therefore, emerges the necessity of developing pointing systems that optimize the alignment between emitter and receiver terminals, maintaining their line of sight and further enhance optical communication. The pointing requirements of a satellite are generally ”beyond the satellite’s body pointing capability” [5], specially in small satellites due to their size, weight and power constraints, requiring fine pointing systems that attain higher accuracies.

1.2 State of the Art

The first FSO communication dates from 1880, when Alexander Graham Bell created the first wireless telephone, the photophone, a device that allowed the transmission of sound modulated onto a beam of light. He was able to transmit a signal wirelessly between two buildings over a distance of 213 m [6]. This aroused a lot of interest to the field of wireless communications, and the invention of the laser, in 1960, has contributed to the advance of FSO technology [7].

The advances in the field of space technology unlocked the door for optical communications in space and emerged the idea of creating an all optical communication architecture to respond to the increasing demand for large capacity and high data rate. FSO technology has developed to the point that today it is possible to transmit high rates of several gigabits per second over many kilometers. Some experimental systems could even ”sustain petabits per second over several meters, and terabits per second over several kilometers in the atmosphere and more in the vacuum of space” [1]. Many experiments have been done to demonstrate the feasibility of optical links, including ground-to-satellite, satellite-to-ground and satellite-to-satellite.

The wavelength division multiplexing (WDM) was first demonstrated in 1999, by using four optical channels, carrying a 2.5 Gbps signal each, over a distance of 4.4 km [8]. This technology allowed to attain higher data rates, for example, in 2009 in Italy, it was reported a 1.28 Tbps intensity modulation/direct detection (IM/DD) based WDM transmission over two buildings that were 210 m apart [9]. Also between two buildings it was demonstrated a dual-polarization transmission using 16 WDM channels, achieving a bit rate of 1.6 Tbps over 80 m [10]. In 2016, a ground-to-mountain link was established at a bit rate of 1.72 Tbps over 10.45 km [11].

Meanwhile, FSO experiments with mobile terminals started being conducted [1]. It was demonstrated a full-duplex communication link between two balloons at 20 km of altitude, attaining a 130 Mbps bit rate and exceeding distances of 100 km [12]. It was also reported the transmission between ground terminal and a moving unmanned arial vehicle (UAV) separated by 50 m, with a 80 Gbps bit rate [13].

It is relevant to mention that in more recent years an interest in quantum key distribution (QKD) applications propelled the development of quantum FSO communications. In particular, the satellite-to-Earth quantum FSO has been a popular subject of study with significant progress [14]. It was demonstrated a free-space satellite-to-ground QKD transmission between Micius satellite and Xinglong ground station,

at a distance of 1200 km. However, the deployment of quantum FSO systems still needs to overcome multiple issues, for example the perturbation that turbulence causes to quantum states.

Further techniques have been developed to improve the performance of FSO systems [4]. At the network or transport layers these techniques include packet re-transmission, network re-routing, quality of service (QoS) control and data re-play, which will not be talked here. At the physical layer these techniques include multiple beam transmissions, increase of the receiver's field of view, adaptive optics systems, relay transmissions, hybrid RF/FSO systems, etc.

Channel coding: Channel coding or forward error correction (FEC) attempts to reduce channel errors induced by the propagation effects, and thus improve the robustness of FSO links. Basically, error coding schemes add redundant information in the data streams, so if some bits are lost or damaged they can be recovered. Some of the schemes proposed specifically for FSO systems are low density parity check (LDPC) codes, convolutional codes, Reed–Solomon codes and turbo codes.

An interesting proposal for FSO is rateless code, which means the receiver does not set a code rate. In [15] it is proposed to set the code rate based on an estimate of the channel conditions, what has revealed to be an efficient strategy to cope with the effects of both weak and strong turbulence.

Diversity: In FSO systems it is common the use of spatial diversity, i.e., having multiple emitters and/or detectors. One simple manner of doing this is sending copies of a signal through repetition coding using different transmitters. They have to be minimally separated (spatially) in order to obtain a diversity gain. On the receiver side, different apertures can collect the signals and combine them. Article [16] shows that this strategy combined with characterizing of turbulent channels as a Log-normal distribution is sufficient to make an intensity modulation/direct detection system efficient.

Adaptive Optics: Adaptive optics (AO) is a technology that aims to mitigate the effects of atmospheric turbulence by minimizing the effect of wavefront distortions. A typical AO system is an array of deformable mirrors, liquid crystals or a digital micro-mirror device. It includes a wavefront sensor, a control system and a wavefront corrector.

However, since the majority of the turbulence effects are tip and tilt, a cheaper and simpler option but still very effective, was thought: a system that consists only of a tip/tilt mirror that corrects the lower-order aberrations and a simple quadrant photodiode that is responsible for measuring the incoming tilt. This is a good solution for FSO systems because the cost of a large-scale deployment of AO using sensors would be too expensive.

Hybrid RF/FSO systems: Pairing an FSO system with a RF system can be very useful to provide high availability under a wide range of weather conditions. Whereas FSO signals are mainly degraded due to heavy fog and resilient to rain, RF signals are mainly affected by rain and not by fog [4], meaning that a RF system can serve as backup when the FSO link is down (even if at a lower capacity). However, the continuous switching between FSO and RF can bring the entire system down.

Relay-Assisted Transmission: This technique uses various relays to link two terminals and is very

effective to oppose the turbulence effects [4]. It works as spatial diversity but only one antenna achieves a very high diversity gain, instead of using several transmitter and receiver apertures. This can only improve performance when the signal-to-noise ratio (SNR) is already high, otherwise the relays will be transmitting replicas with a lot of noise.

The next subsections report some specific studies regarding satellite-satellite links, satellite-to-Ground links and optical satellite networks.

1.2.1 Satellite-Satellite communications

The first laser communication between satellites dates from 2001 [17]. The European Space Agency (ESA) demonstrated a 50 Mbps transmission for optical data-relay services with the satellites SPOT-4 and ARTEMIS. The agency built an optical ground station (OGS) and put Semiconductor Inter Satellite Link Experiment (SILEX) terminals in space. In 2005 it was successfully demonstrated a bi-directional optical link between ESA's ARTEMIS and the Optical Inter-Orbit Communications Engineering Test Satellite, OICETS [18].

In [1] the authors claim that SpaceX Starlink and Telesat intend to improve their satellite constellations with FSO crosslinks in order to provide worldwide broadband internet access. Reporting to [19], SpaceX plans to have 4425 LEO satellites forming a constellation in which the inter-satellite communication will be using lasers to provide "global low-latency high bandwidth coverage". In [17, 20] some inter-satellite optical links were successfully demonstrated. In particular, [20] reports that in 2008 the two LEO satellites TerraSar-X and NFIRE, 5500 km apart and moving at a speed of 25000 km/h, established an error-free optical link at a bit rate of 5.5 Gbps over several seconds.

Being the alignment the major challenge of inter-satellite communication (ISC) due to the mobility of both terminals, [4] highlights the importance of the "implementation of advanced acquisition and tracking mechanisms to ensure transmission reliability". These aim to reduce the pointing errors that come from the vibrations of the satellites.

It will now be discussed the possibility of communicating optically between satellites using LED-based sources, which operate in the visible light band (380 to 750 nm) creating the known visible light communication (VLC) systems. LEDs have been proved to be excellent for space applications due to their ability to bear high temperatures and durability. In [21] the authors suggest a VLC system using LEDs for short to medium range inter-satellite links with pico-/nano satellites, namely CubeSats. This proposal optimizes the relevant design parameters of small satellites for ISC, addressing the size, weight and power (SWaP) constraints, and it is still capable of transmitting high data rates. The deployment of a group of these Cubesats can work as sensor network in space, which promises to be very beneficial for future space missions. The purpose of the study was to evaluate the feasibility and performance of inter-satellite links for different IM/DD schemes taking into account the impact of solar background illumination on link performance. It was concluded that for a transmitted optical power of 4 W and digital pulse interval modulation, with a receiver bandwidth of 3.5 MHz it was achieved a data rate of 2.0 Mbits/s

over a link distance of 500 m at a bit error rate (BER) of 10^{-6}.

The choice of a photodetector for a given application depends on factors like "light power level, wavelength range of the incident light, electrical bandwidth of the detector amplifier, and the mechanical requirements of the application, such as size or temperature range of operation" [21], being the most limitative criteria the cost and the space environment. The works reported in [22, 23] are mentioned because they studied the use of APDs (avalanche photodiodes) and p-i-n photodiodes for VLC systems and general FSO communication. It was concluded that APDs are suitable for situations where the electrical noise in the pre-amplifier is dominant and/or in fiber optic systems, where the signal is weak and the photodiode dark current is the only source of shot noise. Nevertheless, FSO systems deal with large background light and consequently shot noise overpowers the thermal noise. This makes p-i-n photodiodes a more adequate alternative for an FSO detection system.

1.2.2 Satellite-to-Ground communications

Satellite-to-ground (downlink) and ground-to-satellite (uplink) links started being theoretically studied in 1967 [4]. The first experimental demonstration happened some years later with the uplink transmission between a geodetic Earth orbiting satellite-II (GEOS-II) and an OGS (optical ground station), using a ground-based continuous-wave (CW) argon laser [4]. From there on, many theoretical studies were proposed and many experiments were successfully demonstrated [4]. In 1990 it was conducted a relay mirror experiment (RME) with a spacecraft at an altitude of 350 km. Three laser beams were propagated from ground to satellite and then retro-reflected from the RME spacecraft [24]. It was possible to measure the beam intensity profile for further investigations regarding the temporal nature of atmospheric turbulence on the beam. In 1992, two OGS in California and New Mexico transmitted a pulsed laser signal to Galileo optical experiment (GOPEX), establishing an uplink optical communication to deep space vehicle [4]. This uplink proved that atmospheric turbulence is a major cause of beam distortion.

The first uplink and downlink demonstrations date from 1994 by the National Institute of Information and Communications Technology (NICT). They accomplished a bi-directional 1 Mbps link between the Japanese Engineering Test Satellite-VI (ETS-VI) and a ground station in Konegi, Japan. In 1995 it was demonstrated the first bidirectional ground-to-space communication with the ground/orbiter lasercom demonstration (GOLD) [25, 26]. After that, a bidirectional laser link was established between an OGS and the moon, using an AO system to try to reduce the turbulent channel effects [27]. Already in 2013, a sequence of full-duplex communications between a satellite in lunar orbit (approximate distance of 400 000 km) and several ground stations in Spain and USA, were reported by the Lunar Laser Communication Demonstration (LLCD) from NASA, demonstrating bit rates of 20 Mbps for uplink and 622 Mbps for downlink [1]. In 2016, the NICT's Small Optical TrAnsponder (SOTA) was responsible for establishing an optical link communication between a ground station and the LEO satellite SOCRATES, at an altitude of 600 km, attaining downlink data rates of 10 Mbps [1].

Article [28] analyzes the downlink experimental data of two different LEO satellites with the aim to study the received power fluctuations. The data was organized in histograms and compared to some

theoretical probability density functions in order to get a good fit and thus better describe the satellite-to-ground link performance. The first study was done taking into account the data of the Optical Inter-orbit Communications Engineering Test Satellite project - OICETS. In 2008 OICETS was part of a former experiment where a laser beam with a wavelength of 847 nm was used to transmit data stream at a bit rate of 50 Mbps. The specifications of the link can be consulted in Table 1.1. The downlink in study uses the same wavelength of 847 nm with a very narrow laser beam (5.5 μrad) and uses non-return to zero (NRZ) modulation. The transmitted power is 53 mW, a much smaller value than the uplink, since the uplink beacon is much wider.

Parameter	**Uplink**		**Downlink**
	Beacon	**Communication**	
Wavelength	808 nm	815 nm	847 nm
Beam divergence angle	9 mrad	168 μrad	5.5 μrad
Transmitted power	30 W (max)	10 mW	53 mW
Signal coding	CW	2-PPM	NRZ
Data rate	-	2.048 Mbps	49.3724 Mbps
Receiver aperture diameter	26 cmϕ	26 cmϕ	31.8 cmϕ *

Table 1.1: Characteristics of laser communication terminal onboard OICETS, from [28]. * sub-aperture of the 1.5-m telescope.

The second study focused on the data of the Small Optical TrAnsponder - SOTA. This satellite was developed to achieve a reduced system size, weight, and power, like the CubeSats discussed in [21]. It weights only 6 kg and has lower power consumption (under 40 W). The specifications of the link are listed in Table 1.2. SOTA has four different laser sources but for this study only the information of $T \times 1$ (operating at λ=980) and $T \times 4$ (operating at λ=1550 nm) were used. Its tracking and acquisition system is very simple due to the SWaP constraints, so the beam divergence angles are 500 and 168 μrad, much greater than OICETS. The greater divergence guarantees the establishment of the link, even tho there are more pointing errors too. These disadvantages are reflected in the available data rates of 1 or 10 Mbps, lower than the data rate provided by OICETS of $\sim$ 50 Mbps.

Parameter	**Uplink**	**Downlink**	
		$T \times 1$	$T \times 4$
Wavelength	1064 nm	976 nm	1549 nm
Beam divergence angle	300 μrad	500 μrad	223 μrad
Transmitted power (at telescope aperture)	20 W	0.89 MW/sr	0.57 MW/sr
Signal coding	CW	OOK-NRZ	OOK-NRZ
Data rate	-	1 or 10 Mbps	1 or 10 Mbps
Receiver aperture diameter	2/5 cm	1 m	1 m

Table 1.2: Characteristics of laser communication terminals in SOTA experiments, from [28].

The available data from OICETS and SOTA at λ=1550 nm downlinks was organized in histograms and compared to four different probability density funcion (PDF) distributions (Lognormal, Exponential Weibull, Erlang and Gamma-Gamma). The first conclusion was that there are other factors besides the

atmospheric turbulence that affect significantly the link performance, such as clouds, pointing errors, etc. The second conclusion was that, for this particular case, the best distribution fits were obtained for the Exponentiated Weibull and Gamma-Gamma distributions, and the worst fit was consistently the Lognormal distribution. Even though the data was very limited and does not allow any further conclusions, the results can be useful to choose the right PDF in order to simulate an optical downlink.

To finish with the more recent advances, MIT Lincoln Laboratory and NASA are collaborating to develop an optical system that will be installed on a low Earth orbit (LEO) CubeSat to attain a bit rate of 200 Gbps. Then the satellite can ”deliver more than 50 terabytes of information per day to a ground station, as apart of the TeraByte InfraRed Delivery (TBIRD) program” [1].

1.2.3 Networks

Although satellite-to-ground and inter-satellite links were approached individually, it is clear that the ultimate goal is to unify everything creating an optical satellite network of global extent. It is expected that this network revolutionizes space system architectures and might even be used as a critical subsystem, supporting communication services and remote sensing [29].

Article [29] recaps the state-of-the-art of optical crosslink technology, explores architecture implications of the invention of this technology as part of a greater integrated space-terrestrial network, and finishes looking into the improvements that the satellite network can experience, such as performance and cost, and its possible applications. Figure 1.1 represents ”the general concept of an optical space network and its possible user community” [29].

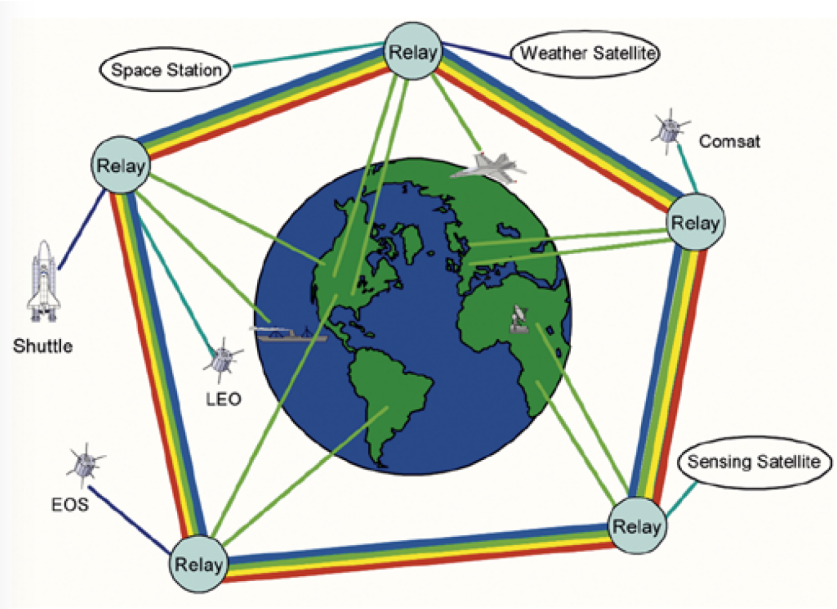

Figure 1.1: General concept of an optical space network and its possible user community, from [29].

The choice of the orbit and the configuration of a satellite constellation depends of the budget and the application. The resulting backbone is expected to ”provide global data networking services, especially in areas of poor or congested terrestrial infrastructure deployment, and in mobile and quick deployment

application scenarios" [29]. To justify the economical viability of an optical satellite network, the authors defend that it ends up being cost-competitive with fiber systems (specially undersea) for long-haul inter-continental communications, constituting a very appealing alternative for terrestrial networks. A fact that supports that is that "in space optical communications the power attenuation due to free-space diffraction loss is only inversely proportional to the square of the link distance, whereas optical fiber attenuation is exponential in distance and amplifiers/repeaters at regular distances are required to maintain performance" [29]. So, the longer the link, the greater the attenuation in the fiber will be when compared with the space optical link, and the optical satellite network becomes viable, even tho its initial cost is higher.

1.3 Objectives

The main objective of this dissertation is to study a closed loop pointing system that optimizes the alignment between emitter and receiver of an optical downlink communication, minimizing the effects of turbulence.

In order to achieve the overall objective it is necessary to attain sectorial sub-objectives, namely:

- Implement a close-loop control system to maximize the alignment of the optical beam;
- Test the pointing algorithms under atmospheric turbulence effects;
- Perspective the feasibility of a long range optical link.

1.4 Thesis Outline

This dissertation is divided into five chapters. The next chapter presents some theoretical background about optical communications and pointing, acquisition and tracking, relevant for a better understanding of satellite optical links.

Chapter 3 starts with an overview of the existing fine pointing systems in nanosatellites and describes the system that will be studied. It depicts the control concepts and the algorithms used to create a closed-loop system, finishing with some simulation work.

In Chapter 4 it is described the experimental implementation, including the laboratory setup, equipment used, experimental data and final results.

Chapter 5 summarizes the obtained results in Chapter 4 and discusses the contributions of the work done and suggestions for future work.

Chapter 2

Optical Communications Background

This chapter gives some background about optical communications system, namely the description of a typical FSO communication system and factors that affect its performance such as modulation schemes, channel noise and atmospheric propagation. Section 2.2 describes a pointing, acquisition and tracking sequence and system.

2.1 Optical communications

A typical FSO communication system is depicted in Figure 2.1. The main components of the system are highlighted, as well as its relevant variables. The transmitter could be a laser diode or a high-intensity light-emitting diode (LED). It produces a modulated beam and transmits it towards the receiver. As it propagates, the beam suffers some losses due to channel effects.

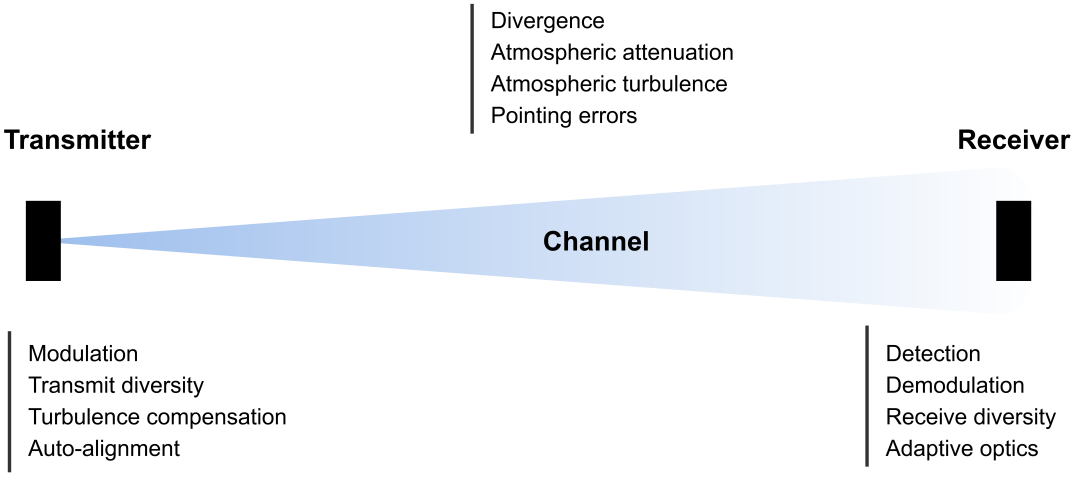

Figure 2.1: Typical FSO communication system, adapted from [1].

To evaluate the performance of the link it can be useful to use the metric signal-to-noise ratio, SNR. According to [28], it can be written as 2.1, where $R(\lambda)$ is the photodetector's responsivity at the operating wavelength, P_r is the received optical power and the parameters σ_{shot} and σ_{thermal} are the shot noise

and thermal noise variances, respectively.

$$\mathrm{SNR} = \frac{S}{N} = \frac{(R(\lambda)P_r)^2}{\sigma^2_{\text{shot}} + \sigma^2_{\text{thermal}}} \tag{2.1}$$

The received power depends on the modulation/demodulation scheme used and on the main channel effects such as beam divergence, attenuation, turbulence and pointing errors.

2.1.1 Modulation and demodulation

The modulation schemes used for optical and RF communications are usually different. While in RF systems information is often encoded both in the amplitude or phase of the signal, in optical sources it is technically easier to perform intensity modulation. The intensity of an optical source varies according to the amplitude of a modulating signal, so the most simple and common method for FSO applications is intensity modulation. Nevertheless, phase modulation is used with optical signals if very high data rates are required. The detection system can be incoherent (more known as direct) or coherent, but usually intensity modulation is associated with direct detection.

Intensity Modulation/Direct Detection systems

Direct detection is performed by a photodetector, allowing the intensity of the optical signal control the amplitude of its electrical signal. Phase modulations can only be detected if the conversion from phase modulation to intensity modulation is performed by an optical interferometry [29]. Some IM/DD schemes are:

- **PAM** or pulse amplitude modulation. Since intensity is directly related with amplitude, we consider this scheme. The data is encoded in different signal amplitude levels. However, since the information is encoded directly onto the amplitude of the signal, schemes such as PAM are adversely affected by intensity fluctuations brought about by the channel [1].

  OOK-NRZ or on–off keying non-return-to-zero is a subset of PAM. The binary ”1” corresponds to the laser being ON and ”0” corresponds to the laser being OFF. Since the encoding is done in the amplitude dimension, it requires a decision threshold at the receiver to make an optimal decision.

- **PPM** or pulse position modulation. The amplitude of a pulse is kept constant and all the pulses have the same width. Then, the positions of the pulses are varied in accordance with the amplitude of the modulating signal. A pulse can occupy L different time positions, so we talk about L-PPM. Unlike OOK, the encoding is done in the time dimension, and thus it is not required a threshold at the detector to make an optimal decision, which makes the format more robust regarding intensity fluctuations. However, a difficulty is the precise time synchronization between the transmitter and the receiver that PPM requires to work correctly.

- **DPIM** or digital pulse interval modulation. Similar to PPM, but each signal begins with a pulse, allowing to remove the unused time slots in between symbols and thus not requiring the PPM time synchronization. The information of a symbol determines its length M (variable). After the pulse

comes k slots of zero power, $1 < k < L$ and $L = 2^M$ [30]. Guard slots can be used to avoid symbols situations where there is no time in between adjacent pulses.

- **SIM** or sub-carrier intensity modulation. It allows modulation formats that also make use of phase, "with some caveats" [1]. First, the information is modulated onto an RF sub-carrier and only then it can be used to drive the intensity of the laser. From here it results the modulated RF sub-carrier. It is common to add a DC bias to the SIM signal, since negative voltages are invalid for laser modulation.

  The information can also be encoded using real-valued orthogonal frequency division multiplexing (**OFDM**) signals. There are two major OFDM techniques: asymmetrically clipped optical (ACO) OFDM, where only odd subcarriers are modulated, and DC biased optical (DCO) OFDM, where both odd and even carriers are modulated [31]. They are characterized by a modulation order M, a number of subcarriers N and a number of guard subcarriers N_g used in the cyclic prefix. These signals are usually used for radio, but can be used in optics too by harnessing Hermitian symmetry. These signals are sensitive to non-linearities but this is not an issue in free space.

The authors of the work reported in [21] analyze a VLC system for inter-satellite communication (ISC), and compared the link performance for five modulation IM/DD schemes: on-off keying non return-to-zero (OOK-NRZ), pulse position modulation (PPM), digital pulse interval modulation (DPIM), DC biased optical OFDM (DCO-OFDM), and asymmetrically clipped optical OFDM (ACO-OFDM). These are suitable for small satellites, since they offer bandwidth and power efficiency, low implementation complexity and robustness to intersymbol interference (ISI). Table 2.1 summarizes the methods to calculate the BER and the bandwidth requirements for each modulation scheme, being R_b the bit rate. It should be noted that the metric BER has been expressed as a function of SNR to facilitate a quantitative comparison and allow a quantitative comparison of the different schemes.

Modulation Scheme	**BER**	**Bandwidth Requirement**
OOK-NRZ	$\frac{1}{2}\operatorname{erfc}\left(\frac{1}{2\sqrt{2}}\sqrt{\mathrm{SNR}}\right)$	R_b
L-PPM	$\frac{1}{2}\operatorname{erfc}\left(\frac{1}{2\sqrt{2}}\sqrt{\mathrm{SNR}\,\frac{L}{2}\log_2 L}\right)$	$R_b\frac{L}{\log_2 L}$
DPIM	$\frac{1}{2}\operatorname{erfc}\left(\frac{1}{2\sqrt{2}}\sqrt{\mathrm{SNR}\,\frac{L_{avg}}{2}\log_2 L}\right)$	$R_b\frac{L_{avg}}{\log_2 L}$
DCO-OFDM	$\frac{\sqrt{M}-1}{\sqrt{M}\log_2\sqrt{M}}\operatorname{erfc}\left(\sqrt{\frac{3\mathrm{SNR}}{2(M-1)}}\right)$	$\frac{R_b(N+N_g)}{\left(\frac{N}{2}-1\right)\log_2 M}$
ACO-OFDM	$\frac{\sqrt{M}-1}{\sqrt{M}\log_2\sqrt{M}}\operatorname{erfc}\left(\sqrt{\frac{3\mathrm{SNR}}{2(M-1)}}\right)$	$\frac{R_b(N+N_g)}{\left(\frac{N}{4}-1\right)\log_2 M}$

Table 2.1: Methods for BER and bandwidth requirements, from [21].

Table 2.2 details the required transmitted optical power to achieve a BER=10^{-6} for each modulation scheme, assuming a link distance of 0.5 km and a bandwidth of 0.5 MHz. L-PPM and DPIM schemes require less optical power than OOK-NRZ to achieve the same BER, with the note that the higher is the level of L, the less optical power is required. Looking to the multicarrier modulation schemes, it can be noticed that they are the ones that require the more optical power to attain the same BER, increasing with M. The authors finish saying that for low to moderate data rates, PPM and DPIM seem to have better error properties than the multicarrier schemes. Nevertheless, for high and very high data rates DCO-OFDM and ACO-OFDM allow bigger capacities and resist more to noise. Concluding, for the purpose of [21], that uses small satellites transmitting at moderate data rates, the DPIM scheme is the more appealing due to its simple receiver structure, good power-efficiency relation and bandwidth requirements.

Modulation Scheme		SNR (dB)	Transmitted optical power (W)
OOK-NRZ		19.6	2.2
L-PPM	L=2	19.6	2.2
	L=4	13.5	1.1
	L=8	8.8	0.6
DPIM	L=2	18.6	1.9
	L=4	14.1	1.2
	L=8	10.4	0.8
DCO-OFDM	M=4	13.5	1.1 + DC bias
	M=16	20.4	2.4 + DC bias
	M=64	26.6	5.0 + DC bias
ACO-OFDM	M=4	13.5	1.1
	M=16	20.4	2.4
	M=64	26.6	5.0

Table 2.2: Required transmitted optical power for link distance of 0.5 km, assumed bandwidth of 0.5 MHz and targeted 10^{-6} BER, from [21].

Coherent detection systems

Coherent systems are more complex than direct detection systems, allowing the usage of more complex formats that use amplitude, phase, frequency, and polarization, such as quadrature phase shift keying (**QPSK**) and quadrature amplitude modulation (**QAM**). Even though their complexity, high sensitivity and need for more signal processing, they might be very useful for long-range systems or for very high data rates [1].

2.1.2 Channel noise

In FSO systems, noise is mainly introduced at the receiver, which can be a photodetector like a PIN photodiode or an avalanche photodiode (APD). Its bandwidth, Δf, is related with the noise power so

that the wider the bandwidth of the detection system, the more noise results.

The main sources of noise are:

- **Thermal noise** or Johnson noise derive from the thermal fluctuations of the electrons in the receiver circuit conducting material. It is white noise, i.e., does not depend on frequency and has Gaussian power spectral density with zero mean and variance given by 2.2 [1]. K_B is the Boltzmann constant, T [K] is the absolute temperature and R is the resistance that includes the shunt resistor associated with the photodetector.

$$\sigma^2_{\text{thermal}} = \frac{4K_BT}{R} \tag{2.2}$$

- **Shot noise** is provoked by the movement of electrons in the photodetector. It describes the random fluctuations over time of the number of detected photons. When operating with large signals, the shot noise can be described by a Gaussian power spectral density with zero mean and variance given by 2.3 [1]. q is the electron charge, P_r is the received optical power and i_d is the dark current of the photodiode.

$$\sigma^2_{\text{shot}} = 2q\left(R(\lambda)P_r + i_d\right) \tag{2.3}$$

The total noise variance is then the sum of two noise variances approximately Gaussian and the total noise power of a receiver without amplification is given by s[1]:

$$P_n = (\sigma^2_{\text{thermal}} + \sigma^2_{\text{shot}})\sqrt{\Delta f}. \tag{2.4}$$

An important metric that accounts both thermal and shot noise contributions is the noise equivalent power (NEP). At the operating wavelength it is given by 2.5 [1], where the value of NEP_{min} can be obtained from the datasheet of the device and R_{max} is the maximum responsivity of the detector.

$$\text{NEP}(\lambda) = \text{NEP}_{\text{min}}\left(\frac{R_{\text{max}}}{R(\lambda)}\right) \tag{2.5}$$

Therefore, the noise power due to the $NEP(\lambda)$ can be calculated by 2.6 [1].

$$P_{\text{NEP}} = \text{NEP}(\lambda)\sqrt{\Delta f}. \tag{2.6}$$

- **Amplifier noise** accounts the noise of the signal (that is now amplified), and the noise added by the amplifier. The total output noise power is given by 2.7 [1], depending of the input noise power P_n, of the gain of the amplifier G and of the noise contribution of the amplifier P_a. Finally this parameter, N, can be used to calculate the SNR and thus evaluate the performance of the receiver.

$$N = P_nG + P_a \tag{2.7}$$

2.1.3 Propagation in the atmosphere

The propagation of a light beam in the atmosphere includes some challenges that may complicate and impair its reception. The main channel impairments summarized in the next subsections are beam divergence, atmospheric attenuation, atmospheric turbulence and pointing errors. All of them should be considered when trying to establish a FSO link and they will have a significant impact in the received power in the receiver.

Beam divergence

When a laser beam propagates its divergence is inevitable. As we can see illustrated in Figure 2.2, the beam leaves the emitter with a certain diameter, and it widens with a divergence angle θ_{div} as it propagates. When it reaches the receiver at a distance L, the diameter is much wider, and thus part of the signal is dissipated and only part hits the detector, resulting in substantial decrease of the received power. However, even though we want low divergences, the use of a larger beam waist can reduce divergence and thus establish longer links.

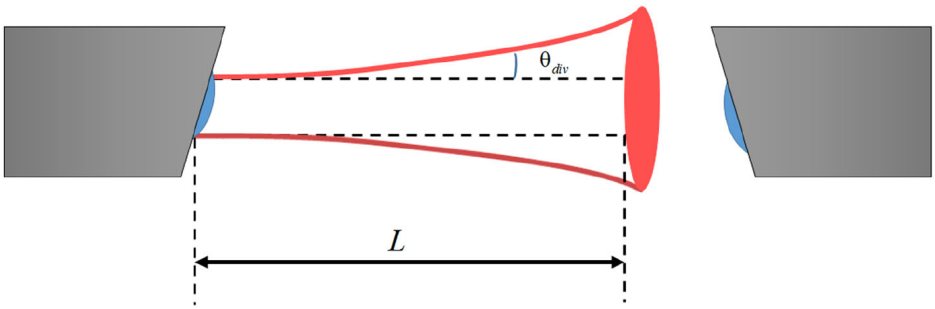

Figure 2.2: Beam divergence illustration, from [1].

Atmospheric attenuation

The propagation of a laser beam through the atmosphere includes absorption and scattering by particles in the medium, depending on their size and concentration. The Beer-Lambert law (expression 2.8) shows the contribute of the overall atmospheric attenuation for the received power. $P_r(z)$ is the power at position z and P_t is the transmitted power by the transmitter. The exponential decay is a function of the attenuation coefficient $\gamma(\lambda)$.

$$P_r(z) = P_t \exp(-\gamma(\lambda)z). \tag{2.8}$$

$\gamma(\lambda)$ describes the absorption and scattering from beam-particles interaction in the atmosphere and it is given by 2.9, where α_{ml} and α_{al} are, respectively, the molecular and aerosol absorption coefficients and β_{ml} and β_{al} are the molecular and aerosol scattering coefficients [1].

$$\gamma(\lambda)[km^{-1}] = \alpha_{ml}(\lambda) + \alpha_{al}(\lambda) + \beta_{ml}(\lambda) + \beta_{al}(\lambda) \tag{2.9}$$

When choosing the wavelength of a FSO system it should be taken into account the atmospheric absorption spectrum. Normally the choice goes to a wavelength that corresponds to minimal absorption and the absorption can be ignored in comparison to the scattering effects.

The attenuation varies significantly according to weather conditions. Table 2.3 summarizes the typical atmospheric attenuation values in various weather conditions for 850 nm and 1550 nm. However, expression 2.9 leads to more precise calculations.

Atmospheric Condition	**Visibility** $[\mathrm{km}]$	**Attenuation** $[\mathrm{dB/km}]$	
		λ = 850 nm	λ = 1550 nm
Clear air	23	0.42	0.2
Haze	4	2.8	1.6
Mist	2	6	4
Light fog	1	13	9
Moderate fog	0.5	28	21
Dense fog	0.2	73	60
Heavy fog	0.05	309	272

Table 2.3: Atmospheric Attenuation for different weather conditions at 850 nm and 1550 nm, from [1].

The scattering can be categorized depending on the comparison between the size of the scattering particles and the wavelength of the incident beam. Rayleigh scattering is due to air molecules smaller than the wavelength, whereas Mie scattering is due to particles that are larger than or comparable to the operating wavelength.

The Rayleigh scattering coefficient can be estimated by 2.10, from the empirical model approached in [32]. N_p represents the number of particles per volume unit and A_p the cross-sectional area of scattering. The authors of [33] say that Rayleigh scattering is negligible for wavelengths beyond 800 nm.

$$\beta_{ml}(\lambda) = 0.827 N_p A_p^3 \lambda^{-4} \tag{2.10}$$

In the case of Mie scattering, its major causes are conditions that affect the visibility like fog and haze. They provoke the scattering of the light mainly in the forward direction. The attenuation due to Mie scattering can be estimated using the empirical model of [34]:

$$\beta_{al}(\lambda) = \frac{3.91}{V} \left(\frac{\lambda}{\lambda_0} \right)^{-q}, \tag{2.11}$$

where V[km] is the visibility range, λ_0=550 nm is the visibility range reference wavelength and coefficient q is the size distribution of the scattering particles and again according to [34] it can take the following values:

$$q = \begin{cases} 0.585 V^{1/3}, & V < 6 \text{ km} \\ 1.3, & 6 < V < 50 \text{ km} \\ 1.6, & V = 50 \text{ km} \end{cases} \tag{2.12}$$

There is still a third scattering type worth mentioning. This last one is induced by particles that are

significantly larger than the operating wavelength such as rain, snow and dust. The attenuation due to rain is given by 2.13 [35], where K_R and α_R are model parameters that depend on the raindrop size and rain temperature, and R [mm/hr] is the precipitation intensity.

$$\gamma_{\text{rain}}[dB/km] = K_R R^{\alpha_R} \tag{2.13}$$

The attenuation due to snow is also given by 2.14 [35], where S [mm/hr] is the snowfall rate , a_S and b_S are snow parameters that depend on whether the snow is wet or dry.

$$\gamma_{\text{snow}}[dB/km] = a_S S^{b_S} \tag{2.14}$$

The attenuation due to dust is given by 2.14 following the empirical model of [36], where V is the visibility, K_d=52 and b_d=-1.05 are model parameters.

$$\gamma_{\text{dust}}[dB/km] = K_d V^{b_d} \tag{2.15}$$

Atmospheric turbulence

The atmospheric turbulence results from air temperature fluctuations that vary randomly in space. The random regions are called cells and when a laser beam propagates through them it suffers aberrations that lead to wavefront distortions and intensity fluctuations. There are two scales to describe the average size of turbulent cells. The first one is an inner scale on the order of millimeters and it is associated with scintillation, a phenomena that seems like ”speckle” on the received beam [1]. The second scale is an outer scale on the order of meters. The outer scale turbulence can cause the beam to corkscrew through the air over long distances which causes beam wander at the receive aperture and leads to fading. Both phenomena are illustrated in Figure 2.3, from [37]. On the right we can see the effect of beam wander, scintillation and both combined in the power receiver at the detector.

Pointing errors

The alignment between emitter and receiver is essential in a FSO system, since misalignment can result in partial or total loss of the signal. This task becomes more challenging if one of the terminals is moving or if the link must operate over long distances. In the particular case of this dissertation, one terminal is fixed (ground station) and the other is mobile (satellite in orbit), with an approximate distance between terminals of 500 km. Some other sources of pointing errors are small earthquakes, thermal expansion and other vibration sources [1].

A very common strategy that aims to reduce pointing errors is the use of an active alignment system. These systems allow that the beam is well collimated when reaching the receiver, which leads to high SNR and consequently a high data rate. According to [38] [39], these systems even can actively correct turbulence-induced tip and tilt aberrations, depending on the design. However, all of this requires that the control system is precise, stable and has microradian accuracy. Another strategy is to expand the

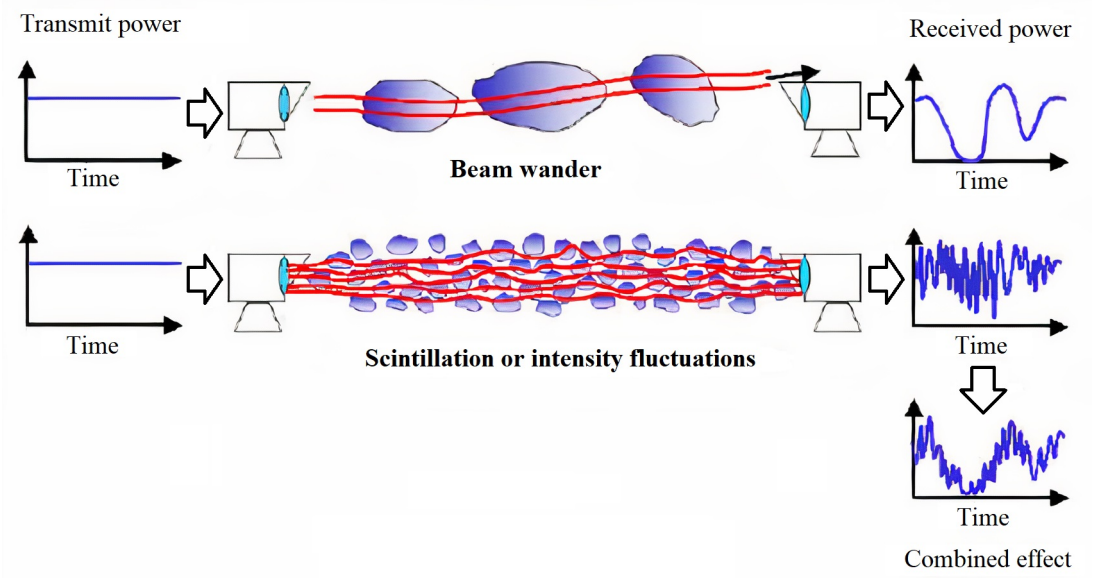

Figure 2.3: Beam wander and scintillation caused by atmospheric turbulence, from [37].

beam by the time it reaches the receiver. This alternative is simple and cheap but very difficult to apply over long distance links due to receiver sensitivity issues.

2.2 Pointing, Acquisition and Tracking

As mentioned before, the alignment between emitter and receiver is essential for the success of an optical communication. A pointing, acquisition and tracking (PAT) system is responsible for searching a laser beam coming from the other terminal and orientate its own terminal in that direction, with the aim to establish a link while tracking the opposite terminal. PAT systems are used in satellites but also in ground stations when very high precision is required.

Figure 2.4 illustrates a pointing, acquisition and tracking sequence:

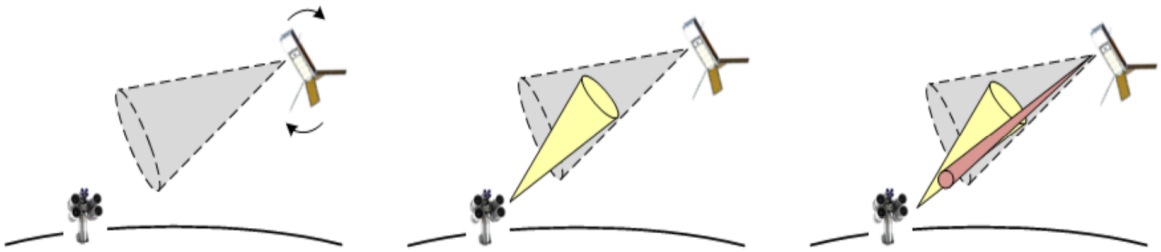

Figure 2.4: Pointing, acquisition and tracking sequence, adapted from [40].

- **Pointing:** In the first phase, coarse pointing is performed, giving a rough estimate of the ground station position. The satellite begins a slew maneuver to point in that direction with the aim that the GS will be visible within the beacon detector's field of view (in grey).
- **Acquisition:** With both terminals roughly aligned, the ground station tracks the satellite and transmits an uplink beacon (in yellow) that will be acquired by the satellite and begin the fine pointing.
- **Tracking:** Fine pointing starts and the beacon is now continuously tracked during the communication window, so the satellite can transmit the downlink signal (in red) towards the ground station.

PAT system

A typical PAT includes a coarse pointing system and a fine pointing system. A very used PAT architecture is a gimbal with an optical bench assembled, including the fine pointing system (FPS) [41]. Still, when dealing with small satellites and their SWaP constraints, it is wise to use directly the attitude determination and control system (ADCS) for coarse pointing, instead of the gimbal. This stage uses a wide field of view detector and thus it does not offer high precision.

The high precision is added to the PAT system with the usage of fine pointing. The key elements of a fine pointing system are a detector and a mobile element to control the alignment of uplink and downlink beams. It can be either a Micro Electro Mechanical System (MEMS) fast steering mirror (FSM) to adjust the downlink signal orientation, or some electromechanic device to control directly the position of the downlink signal.

The most used detectors are cameras and quadrant detectors/quadcells (Figure 2.5).

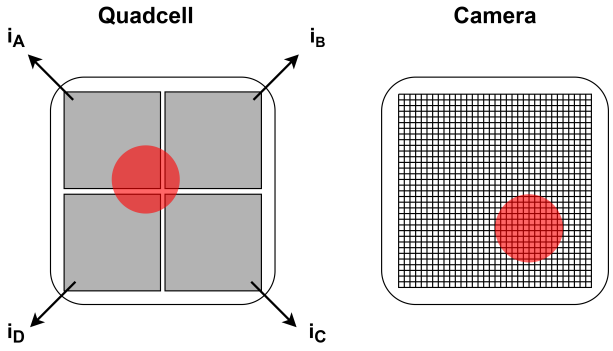

Figure 2.5: Detectors used for fine pointing systems in nanosatellites.

As it can be observed, the quadrant detector is equivalent to a camera of only four pixels. When a laser beam hits a quadrant detector, each quadrant generates a photocurrent, depending on the intensity of the beam in that quadrant. To estimate the position of the beam in both *x* and *y* axes, we can use expressions 2.16 [42].

$$X = \frac{(i_A + i_D) - (i_B + i_C)}{i_A + i_B + i_C + i_D}, \qquad Y = \frac{(i_A + i_B) - (i_D + i_C)}{i_A + i_B + i_C + i_D} \tag{2.16}$$

With the increasing interest in quadcells for beam detectors, studies are developing new methods to improve the detection accuracy of the spot position in quadrant detectors [43] [44]. Their use has shown

to be advantageous as it requires much less processing and memory than a camera.

On the other hand, cameras are more versatile since they are used in satellite missions that include imaging and they serve other beam diagnostic purposes. An image captured by a camera with $M \times N$ pixels gives a full intensity profile, from where it is possible to determine the beam centroid through an image processing algorithm, and thus discover the position of the beam in the image.

Chapter 3

Fine Pointing System

Section 3.1 introduces some fine pointing systems used in nanosatellites recently and section 3.2 presents our fine pointing system proposal, with a detailed description. Section 3.3 depicts the control approach and describes the control chain. Finally, section 3.4 focuses on some simulation tests of the closed loop control system using Matlab Simulink.

3.1 Pointing systems in nanosatellites

In this section we will present and describe some fine pointing systems used in nanosatellites in prior missions that served as a reference for this dissertation.

In 2017, Massachusetts Institute of Technology Space, Telecommunications, Astronomy, and Radiation Laboratory (MIT STAR Lab) developed a precision closed-loop laser pointing system for the Nanosatellite Optical Downlink Experiment (NODE) [5] that was able to attain a 20 μrad pointing accuracy. Its optical diagram is illustrated in Figure 3.1.

The optical diagram shows that NODE receives a 976 nm uplink beacon from the optical ground station that will be detected on a camera and allow to estimate with more accuracy the location of the ground station. Besides that, two internal laser sources are generated: the 1550 nm modulated signal is the downlink beam and the 635 nm is used for calibration. This last one is the main character of the closed loop pointing system, since its sampling on the camera works as direct optical feedback of the FSM pointing angle. However, there is a crucial detail for this system to work that we can observe in Figure 3.2.

After a ray geometry analysis between, the author of [5] identified that the side mirror causes backwards reflection of the calibration beam (in red), explaining why blue and red beams have opposite angles of incidence at the lens when there is optimal alignment. This implies that to have correct pointing, the calibration laser has to have a symmetric relation with the uplink beacon, as shown on the right side of Figure 3.2. The vectors d_B and d_C represent the distance from the uplink beacon and the calibration laser to the center of symmetry, which corresponds to the center of the camera.

The initial demonstration of NODE was a 10 Mbps downlink with a 28 cm diameter amateur telescope

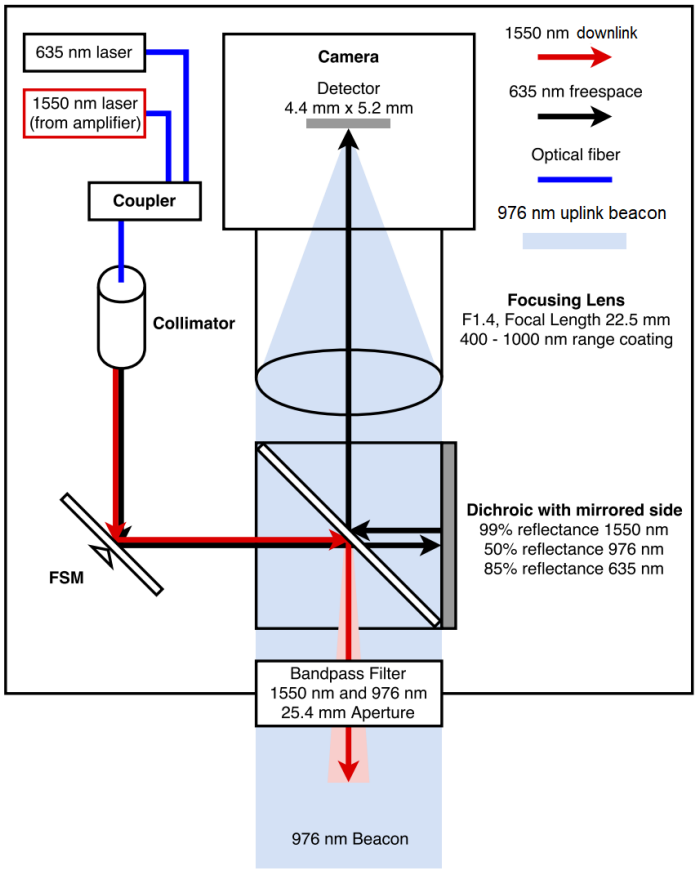

Figure 3.1: Optical diagram of NODE, from [5].

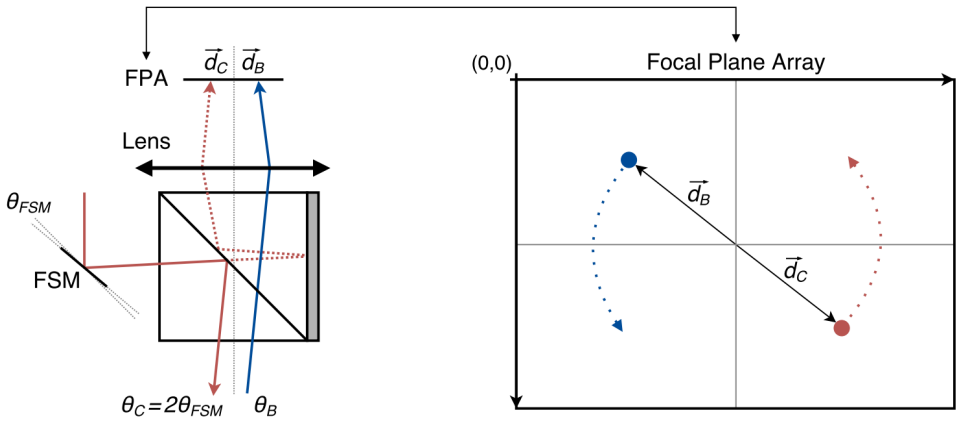

Figure 3.2: Illustration of the ray geometry in the aperture of NODE, where the focal plane array corresponds to a camera, from [5].

from MIT and a 100 Mbps downlink with the 1 m diameter antenna Optical Communications Telescope Laboratory (OCTL) from Jet Propulsion Laboratory (JPL). However, the improvements made on the next NODE generations allowed to attain higher data rates such as a 400 Mbps (generation 2) and more than 1 Gbps (generation 3) downlinks with the JPL OCTL.

In 2018, MIT STAR Lab collaborated with the Precision Space Systems Laboratory at the University of Florida and NASA Ames Research Center in order to develop CubeSats to demonstrate nanosatellite

crosslink and downlink, originating the CubeSat Laser Infrared CrosslinK Mission (CLICK) [45]. Its PAT system includes coarse pointing that uses spacecraft's attitude determination and control system (ADCS), and fine pointing that uses a fast steering mirror with a feedback (integral) control system, allowing high precision. Figure 3.3 shows CLICK's payload optical layout, where there are three optical signals: the 976 nm signal is the uplink tracking beacon (in green), the 1563 nm is the uplink signal (in yellow) and the 1537 nm signal is the downlink signal (in red). The optical design and component selection is deepened in [9]. Their quadcell detector receives the uplink beacon and estimates the beacon spot location. Their alignment method is not explicit but we can see that the downlink signal is fixed and aligned with the dichroic mirrors with an amplitude of 45°. The fine pointing goal is to control the FSM so that the the green and red lasers are overlapped. CLICK was able to demonstrate a 20 Mbps crosslink with a distance of 25 km and a 10 Mbps downlink, at an altitude of 400 km, to the MIT portable opical ground station.

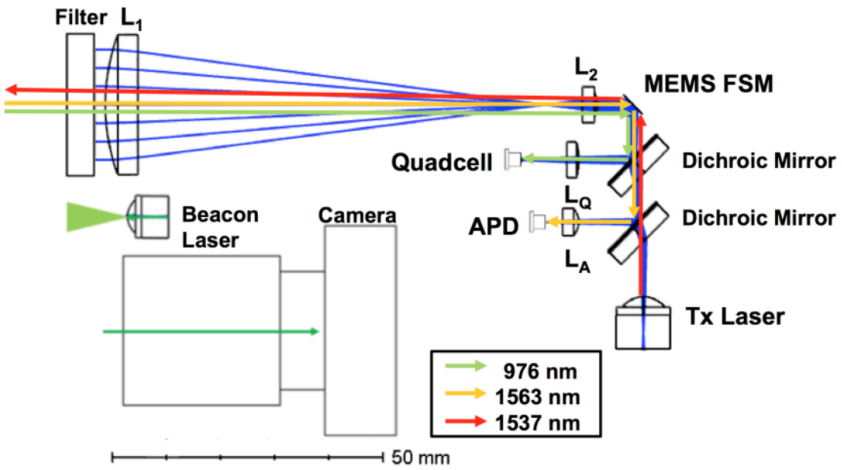

Figure 3.3: CLICK payload optical layout, from [45].

More recently, in 2020 it was developed a high accuracy pointing method (Figure 3.4) that was tested in a satellite-to-ground quantum communication with the quantum science satellite Micius, with demonstrations of 0.5 to 1 μrad pointing accuracy [46].

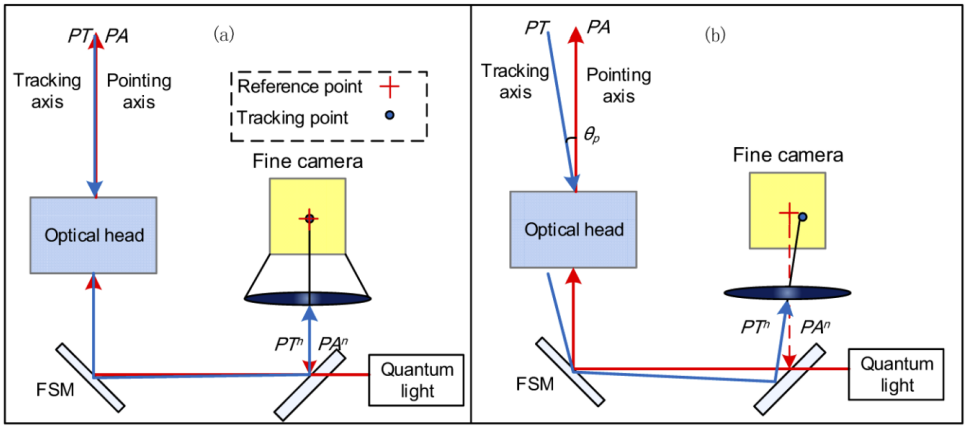

Figure 3.4: Principles of the fine pointing system used on Micius, from [46].

This fine pointing system is similar to CLICK. It uses a quadrant detector and it does not use an internal calibration laser. As it can be observed in Figure 3.4, the two signals involved are: the ground station beacon (blue line) and the downlink quantum signal (red line). When the GS beacon reaches the fine pointing system on the satellite, it is reflected in a fast steering mirror, then in a simple mirror and finally detected by the quadcell. The alignment of red and blue lasers is guaranteed when the FSM is adjusted so that the blue line is on the reference point of the quadcell (Figure 3.4). This way, the downlink signal leaves the satellite with the same direction as the uplink.

3.2 Pointing system proposal

After analysing the two pointing systems presented in section 3.1, and taking into account the required simplicity, the design we came up with is illustrated in a diagram in Figure 3.5. The design is very similar to NODE (Figure 3.1) but there are two major differences. The first one is that only one signal is generated in the satellite. It is a red laser that will be used for calibration, and by being modulated it can simultaneously be the downlink signal and transmit data to the ground station receiver. The second difference is that we do not use a fast steering mirror to control the alignment between uplink beacon and calibration beam. Instead, we assemble our laser on a kinematic mount that allows to control directly the position of the laser.

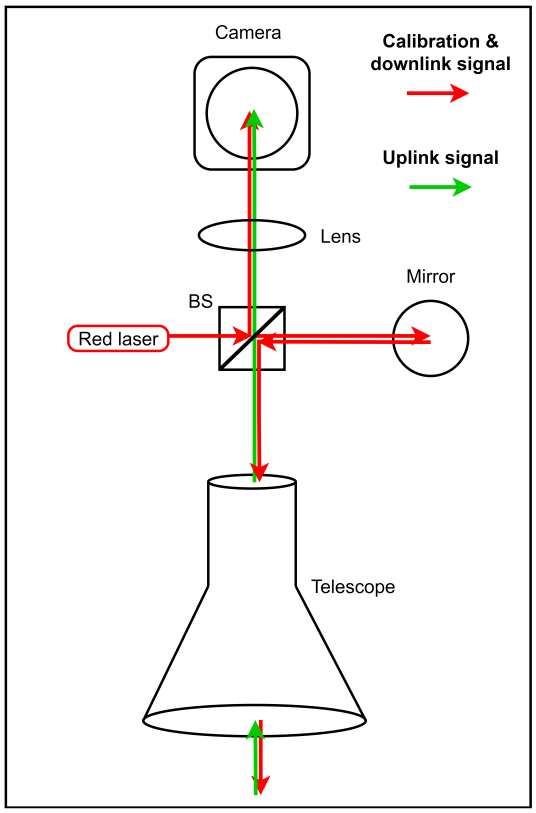

(a) Optical diagram.

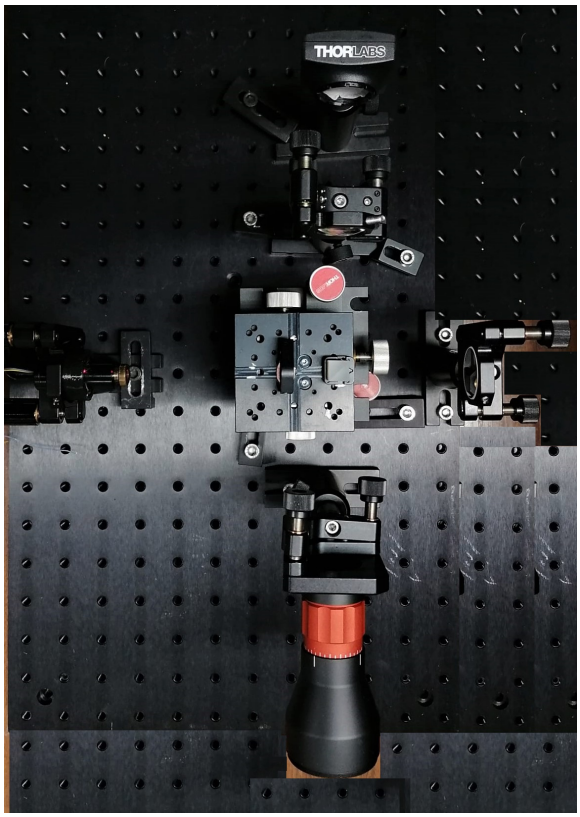

(b) Experimental assembly.

Figure 3.5: Pointing system proposal.

Looking at Figure 3.5 (a), we see the uplink beacon (in green) coming from the ground station and reaching the satellite. It passes the telescope, where its size is reduced, then it is transmitted through a beam splitter, it passes a lens where it is focused, and it is finally detected on the camera. At the same time, the calibration laser (in red) hits the beam splitter and half is reflected to the camera. We are now able to compute the distance between green and red spots and adjust the position of the calibration laser in order to be aligned with the uplink beacon in the camera. The closed loop control concept and developed algorithms will be described with more detail in the next section 3.3. However, the other half of the red signal (modulated) is transmitted through the beam splitter and reflected in a simple mirror, coming back to the beam splitter and then reflected to the telescope. When the lasers are aligned, the downlink signal leaves the satellite with the exact same orientation as the uplink beacon, going toward the ground station, where it is detected.

3.3 Closed Loop Control

The pointing objective is to follow a dynamic reference, in this case, the uplink beacon disturbed by atmospheric turbulence. The diagram in Figure 3.8 represents the closed loop control pointing system. The fine pointing begins when the camera acquires an image containing green and red laser beams. Their centroids in the image (in pixels) are calculated by an image processing algorithm. However, the device that controls the calibration laser position works with positions in millimeters, so the centroids suffer a transformation to be converted to millimeters. The difference between green and red centroids is the pointing error and the correction to apply is determined by the controller. All of these steps are explained in more detail in the next subsections.

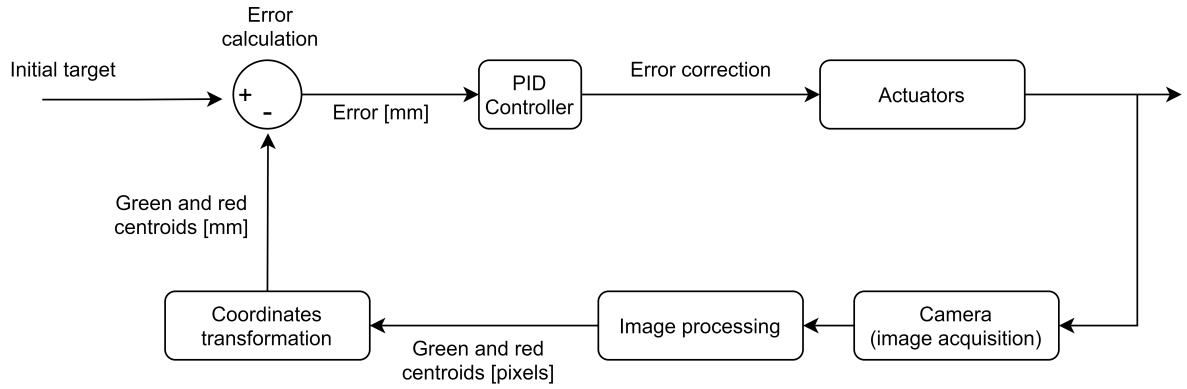

Figure 3.6: Closed loop control system.

We chose to use a proportional, integral and derivative (PID) controller. The error feeding the closed loop corresponds to the difference between the reference (uplink beacon centroid) and the variable measured in the loop (calibration laser centroid). The correction applied is given by equation 3.1 [47], where $p(t)$ is the new position and p_0 is the current position of the calibration laser, K_p, K_i and K_d are

the proportional, integral and derivative gains of the controller and $e(t)$ is the error.

$$p(t) = p_0 + K_p e(t) + K_i \int_0^t e(\tau)\mathrm{d}\tau + K_d \frac{\mathrm{d}e(t)}{\mathrm{d}t}, \tag{3.1}$$

Proportional control is related to the amplitude of the error. When the error is large, the proportional term is responsible for applying a large correction. When the error is smaller, the correction is small. Integral control calculates the summation of the error (integral), what gives it an overview of the error over time. When the error is small, the proportional response is also small and may not have enough force to apply the exact right correction. The integral term adds the extra correction, allowing the response to be faster. Finally, derivative control cares about the rate of change of the error, and not the error itself. The faster the error changes, the larger the derivative becomes. Its intend is to smooth the error over time. This way, a combination between proportional, integral and derivative can bring a faster and less aggressive response of the system.

Active control

The fine pointing begins when the camera takes one frame. The frame will have a dark background, the green and red laser beams (visible in Figure 3.7). After image acquisition, it necessary an image processing algorithm to identify the beams separately and calculate their centroids. The algorithm developed in Matlab starts by removing the background of the image and apply a red mask, meaning only areas of the image with a big intensity of red will be considered. Then the largest blob is extracted, to make sure we are looking at just one red spot. Finally, we can use the Matlab function ”regionprops” that computes the center of mass of a region, returning the *x* and *y* coordinates (in pixels) of the centroid of the red blob. The process is then repeated for the green beam, using a green mask and getting the green beam centroid.

We have now the two centroids coordinates. However, the device that controls the position of the red laser moves x millimeters in the horizontal axis and y mm in the vertical axis, so it is important to determine a correlation that tells us when we move the laser 1 mm, how many pixels the centroid will be dislocated. This procedure was performed experimentally in section 4.2 and it concludes the correlation can be described as a linear:

$$\text{centroid [pixels]} = m \times \text{laser position [mm]} + b. \tag{3.2}$$

Now that we know the position of the laser (in millimeters) that correspond to the computed centroid, we can proceed to calculate the error illustrated in Figure 3.7. As we are working with a bi-dimensional system, the total error is given by the square-root of sum of x and y errors squared.

It corresponds to the distance between centroids:

$$\text{error} = \text{target centroid} - \text{calibration centroid}. \tag{3.3}$$

The final step of the fine pointing loop is to apply a correction to the calibration laser position with

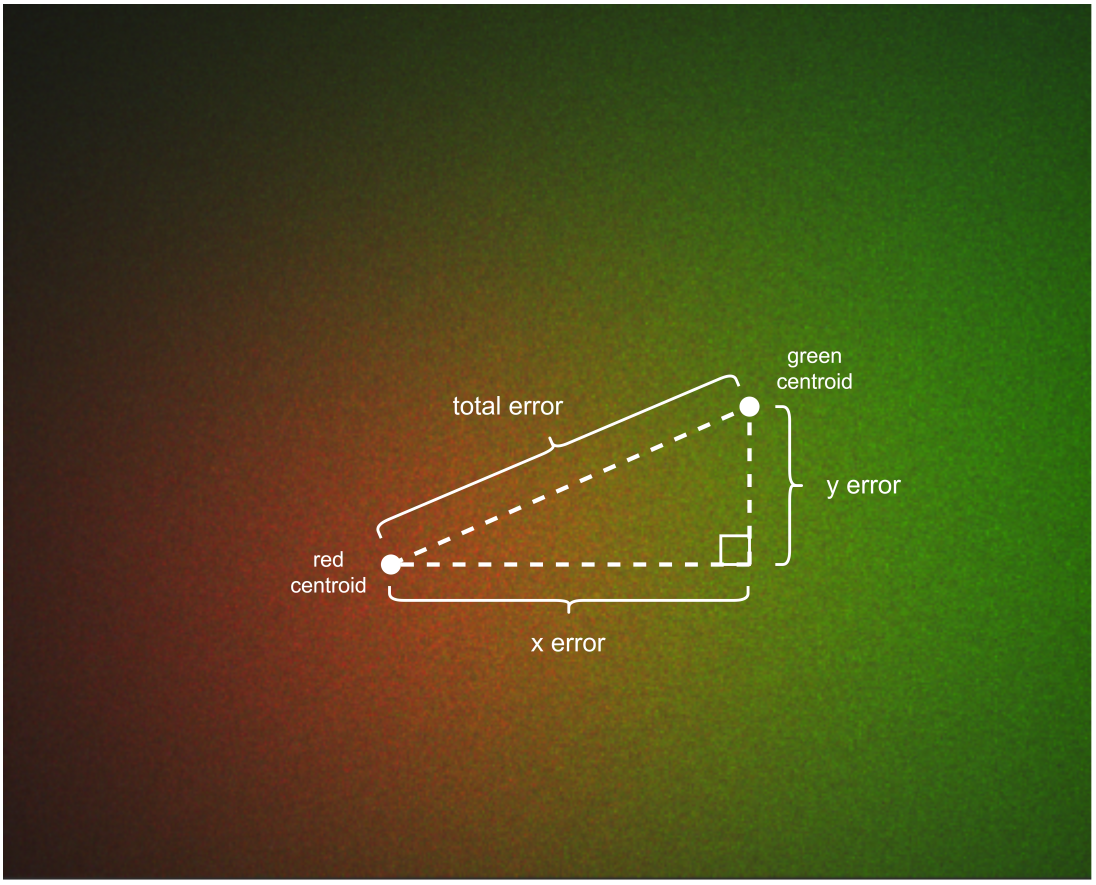

Figure 3.7: Illustration of the alignment error. It corresponds to the distance between red and green spots in x and y axes.

the aim to align it with the target, or at least bring them closer. The correction can be just adding the error to the red laser current position, nevertheless, when using PID control, the expression of the new position has to include the proportional, integral and derivative terms in 3.1. The choice of the gain values, integral and derivative of the error will be done experimentally in section 4.2.

3.4 Modelling and simulation

In order to better understand the control loop it was essential to do some simulation work. This allows to model the dynamic elements of the control chain such as the camera, the controller and the kinematic mount responsible for moving the calibration laser, and see their influence in the loop. The closed loop control system was created using the Matlab Simulink environment and it is represented in Figure 3.8.

Since we could not determine a transfer function for our kinematic mount, we considered the usage of the FSM used in the NODE simulation scheme [5]. The first dynamic element of the loop is the camera. It works at a certain sampling rate, however, the FSM's dynamics are much slower, making them the most limiting element of the system and thus the focus of the model. Nevertheless, image acquisition and processing can influence significantly the loop, due to noise that gets to the camera and to the time delay caused by the centroid computation.

Moving to the FSM, its model is simple, since their manufacturer gave an exclusive datasheet, where

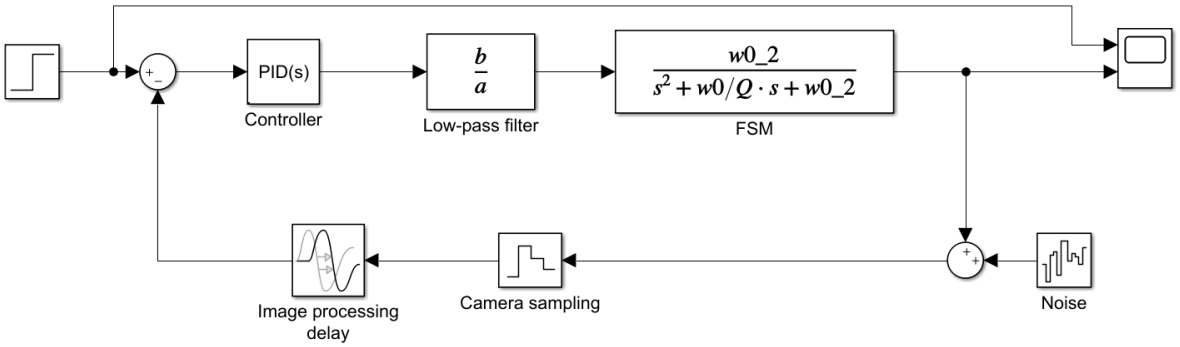

Figure 3.8: Closed loop system created in Matlab Simulink.

the FSM specifications needed to determine its transfer function are discriminated, such as resonant frequency w_0 and quality factor Q. The dynamic model is given by second order transfer function, where the input is a driving voltage and the output is the new angular position of the FSM:

$$\frac{\theta_{FSM}(s)}{V_{driving}(s)} = \frac{w_0^2}{s^2 + \frac{w_0}{Q}s + w_0^2}, \tag{3.4}$$

It was verified that the FSM step response was extremely ressonant, so to fix this it was placed an analog low-pass filter at the FSM entrance. The filter used in [5] is a 6-th order Bessel LPF and its cut-off frequency is 200 Hz. In the low-pass filter block in Figure 3.8, ”b” and ”a” are transfer function coefficients. The comparison of the FSM step response with and without the filter is presented in Figure 3.9.

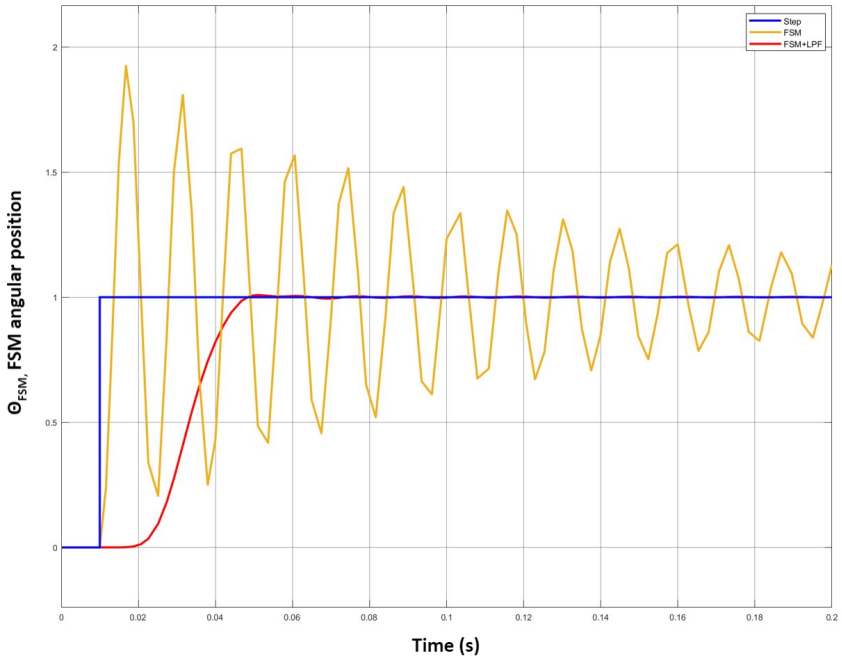

Figure 3.9: Step response of the FSM and of the FSM + low-pass filter.

At last, we used the Simulink Control Design Toolbox to tune the PID controller. In Figure 3.10 it is

shown the closed loop system response to a step.

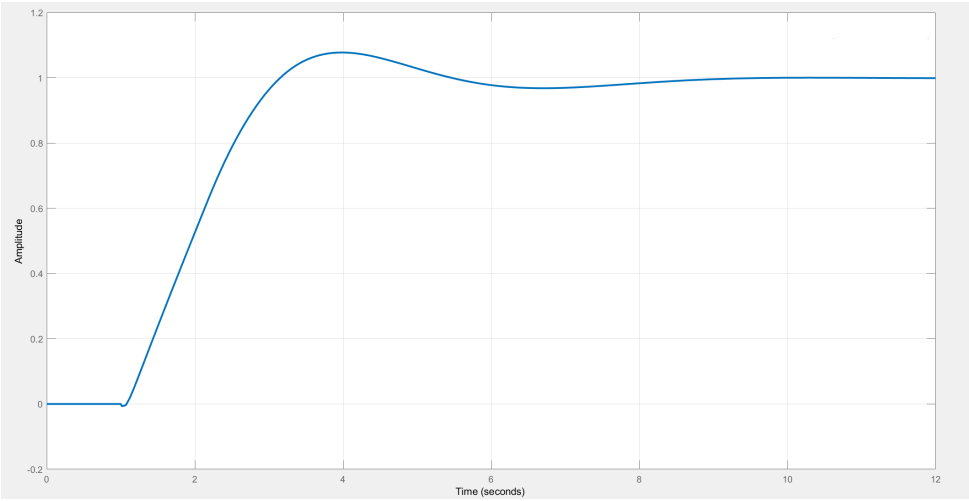

Figure 3.10: Step response of the closed loop system created in Matlab Simulink.

The definition of the proportional, integral and derivative gains have significant impact in the way the system responds and adapts. They make the response faster or slower, more robust or more aggressive. For this particular case, the automatic tuning suggested the best gain parameters to be K_p=0.1471, K_i=0.5111 and K_d=-0.2236.

Chapter 4

Experimental Implementation

This chapter describes the laboratory setup assembled to validate the control algorithms and test the control system. In Section 4.1 we can find the description of the experimental setup and the list of equipment used to assemble both satellite and ground station. Next, Section 4.2 depicts the experiment, showing the experimental results of the calibrations mentioned on Section 3.3. Finally, section 4.3 presents and analyzes the experimental results.

4.1 Experimental setup

An experimental testbed is essential to test and validate the control algorithms in a more real situation. The setup is represented in a diagram in Figure 4.1. On the right side we have the block representing the optical ground station, which we consider to be the emitter, and on the left side is the satellite receiver. The uplink beacon (in green) is transmitted from the ground station to the satellite, entering the telescope and being detected on the camera. Then the control algorithms are performed for alignment. Once this happens, the red modulated laser is reflected in a simple mirror and leaves the satellite with the same orientation as the green laser. This downlink signal is then received at the ground station's detector.

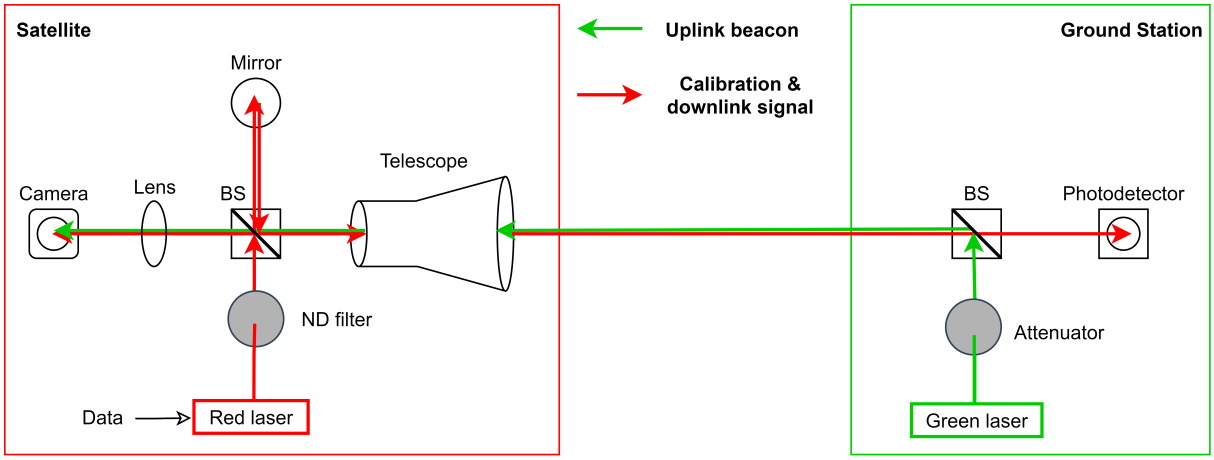

Figure 4.1: Diagram of the setup assembled in the laboratory.

The real setup assembled on the laboratory is shown in Figure 4.2. It is important to mention that all optical components were manually mounted and aligned on the optical board, which can lead to major alignment errors.

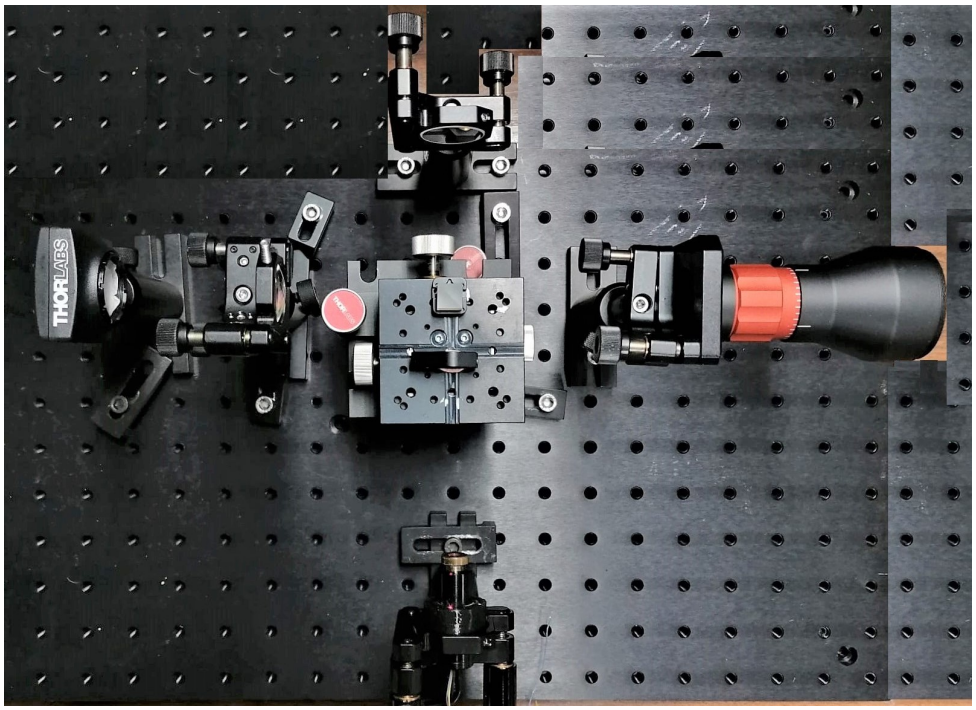

(a) Satellite's fine pointing system.

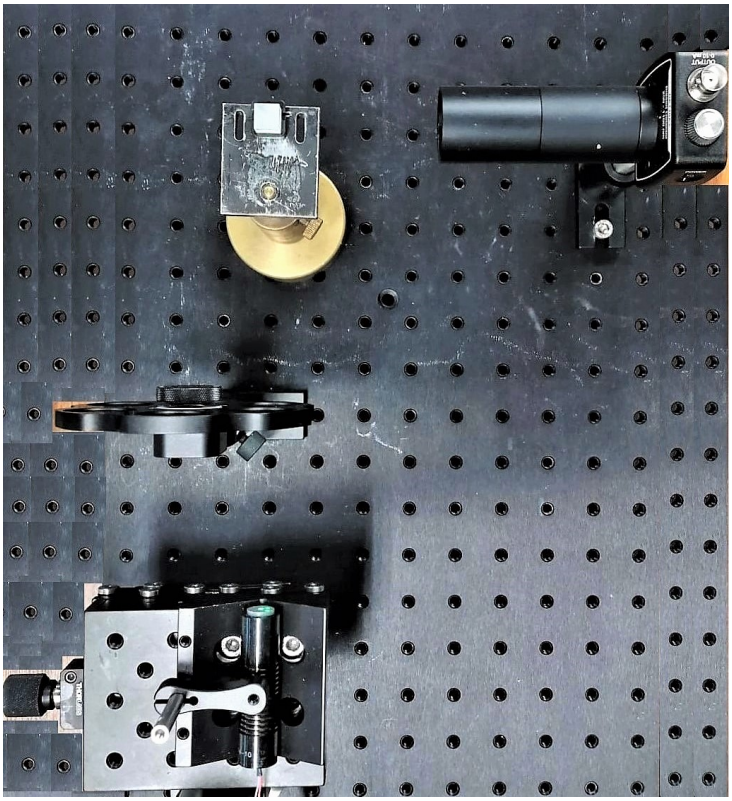

(b) Optical ground station.

Figure 4.2: Experimental setup.

The optical ground station corresponds to Figure 4.2 (b) and it comprises the uplink beacon, a beam splitter from Thorlabs with a 50:50 beamsplitting ratio, an attenuator that is a 1.0 optical density absorptive neutral density (ND) filter to reduce the intensity of the transmitter laser when it hits the camera on the satellite, and a detector. The detector used was the Thorlabs DET10A2, which is a biased silicon detector with an active area of 0.8 mm^2 and a wavelength range from 200 to 1100 nm, adequate to detect the red laser. It is positioned on the ground station to receive the downlink signal and then connected to an oscilloscope so the downlink reception is confirmed.

Figure 4.2 (a) shows the assembly of satellite fine pointing system. On the bottom we see the telescope and another Thorlabs 50:50 beam splitter. On the left we have the downlink and calibration laser assembled on its kinematic mount that is operated by two controllers and stages (one for each axis) that are not visible in the figure. Between the laser and the beam splitter there is a 1.3 optical density absorptive ND filter, responsible for attenuating the intensity of the red laser so it does not saturate the camera. On the right we see the simple mirror responsible for reflecting the red laser for it to follow its path towards the ground station. Finally, on top, we have the tracking camera and added a convex lens from Thorlabs with a focal distance of 3 cm, with the purpose of reducing and focus the beams. Otherwise, their spots would be very large when they reach the camera.

Required equipment

- **Uplink beacon:**

  For the uplink beacon from the optical ground station it was considered a Roithner green laser working on 520 nm with a power of 5 mW. This power is too high to be detected on the camera, causing full saturation of the image, and thus the 1.0 optical density absorptive ND filter and the convex lens are used, to reduce the intensity and the size of the beam, respectively.

- **Telescope:**

  The uplink beacon is very large when arrives to the satellite, so the objective of the telescope is to reduce its size, keeping the collimation. The Thorlabs Fixed Magnification Beam Expander GBE05-B has 5X beam reduction.

- **Downlink signal:**

  The satellite laser is a 40 mW 650 nm laser from Roithner. It supports transistor-transistor-logic (TTL) modulation, so we used an arduino to modulate it by just switching it on and off, and thus transmit data as a downlink signal. At the same time, its main function is the internal calibration. The laser is detected on the camera and it follows the green laser, aiming to keep receiver and emitter aligned.

- **Precision kinematic mount, controllers and stages:**

  The red laser is assembled on a Thorlabs Precision Kinematic Mirror Mount KS2 in order to control

its position. This mount holds 50.0 mm optics and has 3 adjusters, allowing angular adjustment of ±4 °in x and y axes.

The controllers and stages are responsible for controlling the two axes of the kinematic mount. The chosen model was Thorlabs Kinesis® KDC101 K-Cube™ Brushed DC Servo Motor Controller. They allow manual and/or automatic control of DC Servo motors using their own motion control software Kinesis or in this case, using Matlab. The dimensions of 60.0 x 60.0 x 49.2 mm are highly compact and thus suitable for small satellites.

The compatible stages are the Thorlabs Z812. They will actuate on the kinematic mount and have a total range of 12 mm in each axes and a maximum velocity of 2.6 mm/s.

- **Tracking camera**

The chosen model for the camera was the Thorlabs DCC1645C USB 2.0 CMOS Camera in Figure 4.3, with some of its characteristics are summarized in Table 4.1. It has its own software called Thorcam that can be controlled with Matlab.

Figure 4.3: Thorlabs DCC1645C USB 2.0 CMOS Camera.

Camera specifications	
Sensor type	Color
Effective number of pixels	1280 x 1024
Imaging area	4.61 mm x 3.69 mm
Pixel Size	3.6 μm (square)
Optical Format	1/3”
Max Frame Rate	24.9 fps
Power Consumption	0.3 - 0.8 W

Table 4.1: Specifications of the Thorlabs DCC1645C USB 2.0 CMOS Camera.

The satellite detector is a very important element of our system. It is responsible for detecting both uplink beacon and calibration laser. In this case, the imaging area of 4.61 mm x 3.69 mm is very small, which is why it was so important to insert the convex lens before the camera. To avoid saturation of the acquired images, it was placed a piece of tracing paper right in front of the detector. This method allowed to cut some of the intensity of the beams without using another attenuator.

4.2 Experimental implementation

After the setup assembly, it is finally possible to test the closed loop control system described in section 3.3 and demonstrate downlink reception in the ground station.

The first step was to connect and configure the hardware (camera, controllers and stages) using Matlab. We started by testing the range of positions of the red laser that are detected within the camera's field of view and concluded that the beam is present in the image when the controller position is between $x \in [0.6, 3.2]$ millimeters and $y \in [0.2, 2.1]$ millimeters. As we mentioned in section **??**, we determined a

correspondence between the kinematic mount x and y position [mm] and the projection of the red laser on the camera [pixels], presented in Figure 4.4.

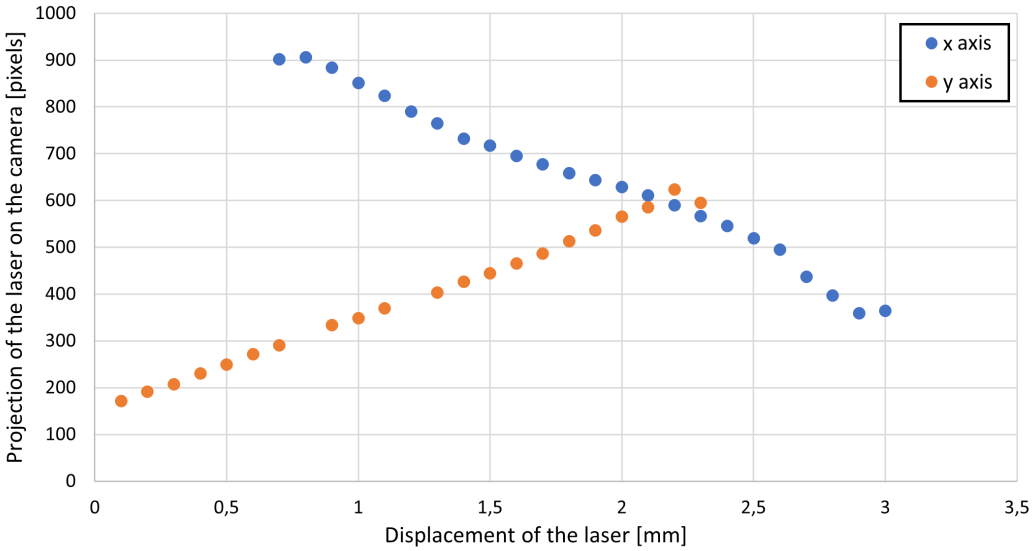

Figure 4.4: Projection of the red laser on the camera as a function of its displacement done by the kinematic mount.

The correlation is linear and it has value of 277 for the x axis and 201 for the y axis, meaning that when we dislocate the laser 1 mm vertically, its projection in the camera will be displaced 201 pixels in the same axis.

Before passing to the control algorithm tests, it is important to mention that at an early stage, it was only assembled the satellite setup, meaning there was no uplink beacon. For this reason, the first tests were performed using random targets created in Matlab: for each iteration of the control loop, it was generated a random centroid target that falls within the pixel dimensions of the image took by the camera (pretending to be the uplink beacon). Of course this does not represent a real situation because the uplink beacon is expected to move around so randomly. Still, these tests served to verify if the system responded to alterations of the target position. At a second stage, when the ground station was assembled, it was tested the image processing algorithm to detect and calculate the green centroid. However, the green laser was static, so we could not use it as a dynamic target for the fine pointing system. Only in a final stage, we were able to simulate a turbulent environment and perturb the laser beam. We used 3 lamps of 100 W each connected to power supply, illustrated in Figure 4.5. The green laser passes right above the lamps and their overheating provokes disturbance of the beam, just like the uplink beacon is disturbed when it passes the atmosphere towards the satellite.

After defining the useful range of the controllers, determining the correlation between position of the laser and its projection on the camera and having a dynamic uplink beacon, it is now possible to start testing the algorithms. When the control loop starts, the camera acquires an image similar to Figure 3.7, with a red and a green spots. It goes through image processing to estimate the centroids of the spots. The green centroid is set as the reference and the error is computed through expression 3.3 in both x and y axes. It is convenient to present the pointing error in radians, so Figure 4.6 helps to understand

Figure 4.5: Simulation of the atmospheric turbulence: three 100 W lamps heat the uplink beacon propagation region, causing disturbance of the beam.

the principle of the conversion from millimeters to radians, where L is the distance from the emitter to the telescope and Δx is the range of positions of the laser that the camera can detect.

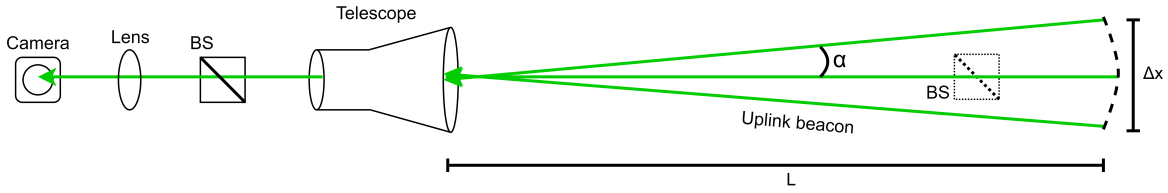

Figure 4.6: Scheme of the distances measured to find the α angle that allows to convert [mm] to [rad].

After measuring the distances, it was concluded that the proposed system allows corrections until of 2α = 3.4 mrad. For a LEO-to-ground communication, where L=500km, the pointing range Δx at the Earth surface will be around 0.5 km, which is much higher than the receiver telescope.

The last step of the control loop is to calculate the correction and actuate, changing the position of the calibration laser to follow the reference. The correction calculation depends on the type of control. At first, it was tested the simpler approach which is proportional control. With a proportional gain K_p of 1, it was assumed that the new position to where we want to move the red laser beam is the sum of its current position with the error value. After some initial tests, we advanced to PID control and used expression 3.1 to estimate the correction to apply. To calculate the integral and the derivative terms of the expression, it was considered the plot of the *x* error over time obtained with proportional control and K_p=1 (plot available in section 4.3). The values considered for *x* axis were $\int_0^t e_x \mathrm{d}\tau$ = 0.1190, $\frac{\mathrm{d}e_x(t)}{\mathrm{d}t}$ = 0.0027, and for *y* axis were $\int_0^t e_y \mathrm{d}\tau$ = 0.0089 and $\frac{\mathrm{d}e_y(t)}{\mathrm{d}t}$ = 0.0198. With these values fixed, we varied

the gain values K_p, K_i and K_d between 0.1, 1 and 10 to see their clear influence in system response. All the results obtained will be presented and analyzed in the next section 4.3.

4.3 Experimental Results

4.3.1 Control Tests

In this section we will present the results of the tests performed, always running the control system for 100 cycles. We thought it was interesting to start testing a system that does not use control (Figure 4.7), that is, it receives the uplink beacon from the ground station but it does not move in response to it. The error measured is the error between the green beam and the center of the detector.

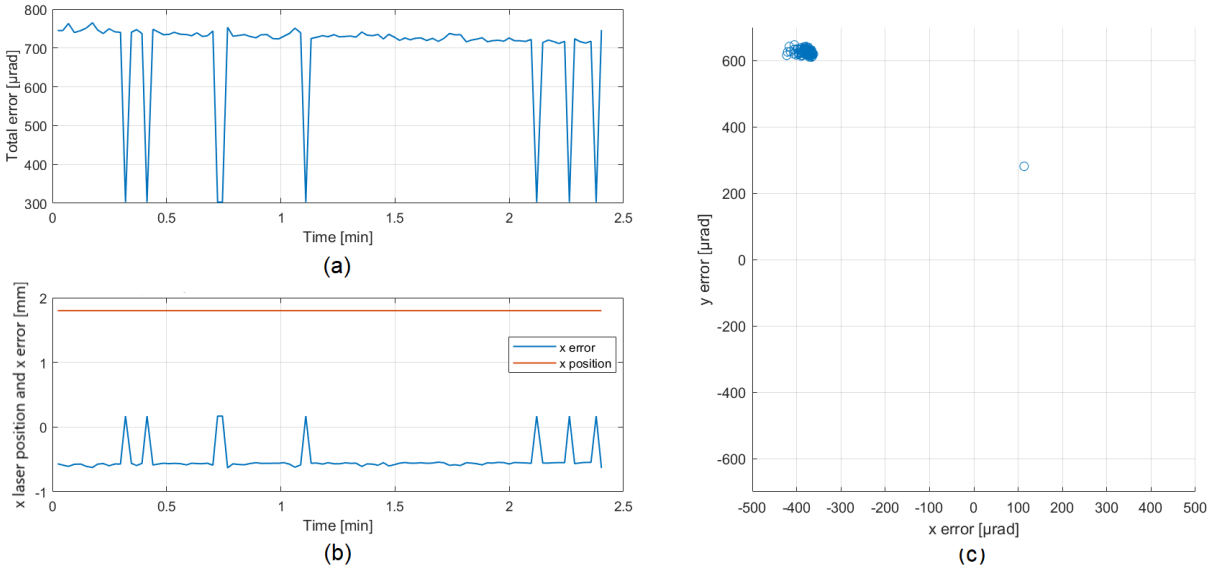

Figure 4.7: (a) Total pointing error, (b) *x* position of the calibration laser and *x* error over time and (c) scatter plot of the error when the FPS does not use any control.

The fact that the *x* position of the red laser (in orange) is static means exactly that the calibration laser does not move in order to follow the uplink beacon. The total pointing error over time has a mean of 697 µrad and scatter shows the error is always very far away from zero.

The simpler control approach is the **proportional control**. To test it (Figure 4.8), we used a proportional gain K_p=1, meaning the correction to apply is equal to the error.

As we can see in Figure 4.8, the *x* error oscillates around zero. The total pointing error mean is 42.5 µrad, which is more than 10 times less than the previous approach that does not use control. We can also see that every time the beam is disturbed due to turbulence, the system corrects it, bringing the error for lower values again.

We will now analyze the results of studying the variation of the proportional, integral and derivative gains using a **PID control** system. We gave the gains the values 0.1, 1 and 10 and examine the difference it makes to the system response. The same way as before, we ran the control loop for 100 cycles.

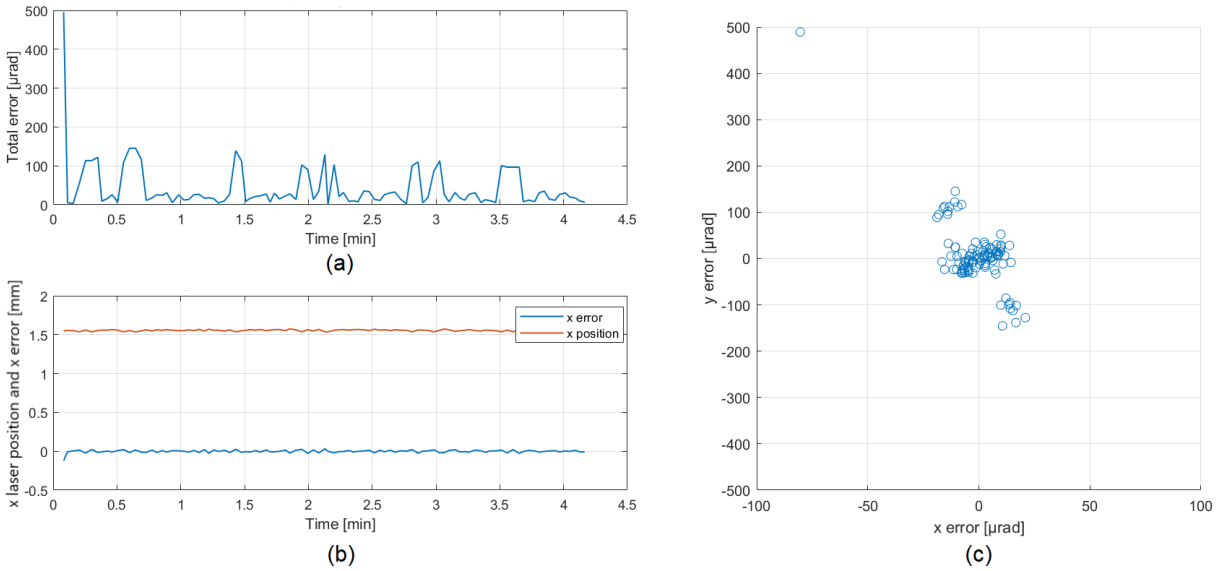

Figure 4.8: (a) Total pointing error, (b) *x* position of the calibration laser and *x* error over time and (c) scatter plot of the error when the FPS uses proportional control with $K_p = 1$.

To study the effects of the proportional gain K_p, we fixed K_i=K_d=0.1. The total error, *x* position of the calibration laser and *x* error when (a) K_p=0.1, (b) K_p=1 and (c) K_p=10 are presented in Figure 4.9.

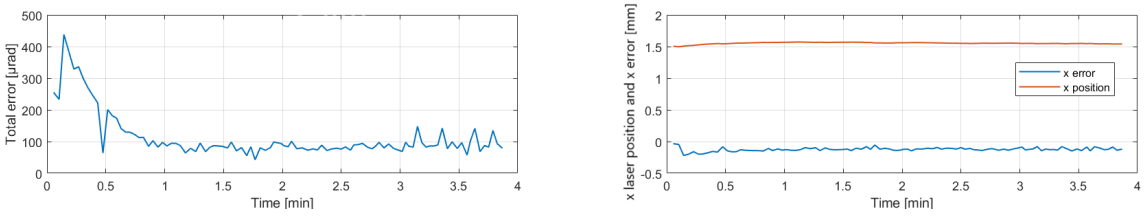

(a) K_p=0.1, K_i=0.1 and K_d=0.1.

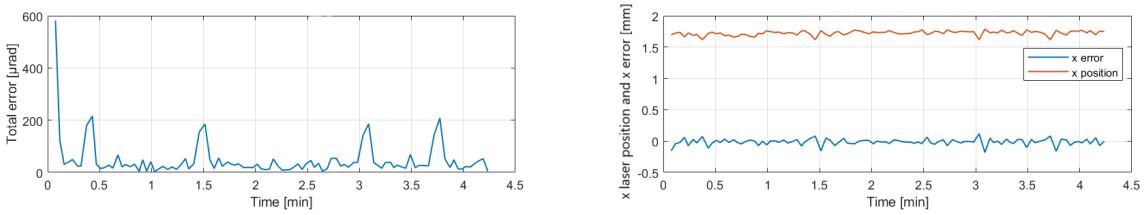

(b) K_p=1, K_i=0.1 and K_d=0.1.

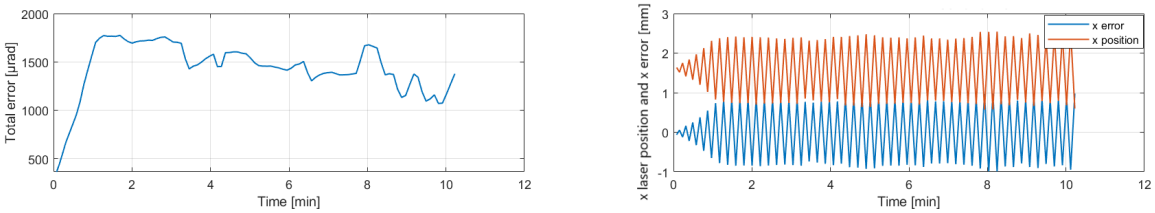

(c) K_p=2, K_i=0.1 and K_d=0.1.

Figure 4.9: Total error, *x* position of the calibration laser and *x* error over time, when K_p increases.

In (a) we can see that the system is slower to respond, only stabilizing after 1 second, with a mean total error of 112.5 µrad. Since the correction applied to the calibration laser is proportional to the error,

this low K_p barely makes the position of the laser move. The correction is very small, so it never corrects as much as needed, and that is why we can see the *x* error oscillating around -0.1, instead of 0. In (b) we get the fastest response, and the lowest mean total error: 45.7 µrad. We see some disturbances but the system is able to correct them, bringing the error to lower values again. The calibration laser position is not as smooth as in (a) but this time, the *x* error oscillates around zero, implying that there is alignment of the red and green lasers. For the highest K_p value, we tried 10, 5 and 2, and as we can see in (c), K_p=2 still causes a poor response of the system. The response is slow and the mean total error increases significantly to 1425.2 µrad. The slowness is due the opposite motive as in (a). The correction to apply is so big that the calibration laser moves a lot to correct the error. The program takes a lot more time to run the 100 cycles, and even though the *x* error oscillates around zero, the values it takes are more extreme, meaning the error between the lasers always exists.

Therefore, lower proportional gains do not have enough strength to correct the error completely, but rising K_p too much generate inadequate corrections and makes the system much slower. The test where K_p=1 is the most adequate to follow the reference quickly and to guarantee the alignment.

To show a good example of what happens when we increase the integral gain K_i, we fixed K_p=1 and K_d=0.1. In Figure 4.10 we observe the total error, *x* position of the calibration laser and *x* error when (a) K_i=0.1, (b) K_i=1 and (c) K_i=10.

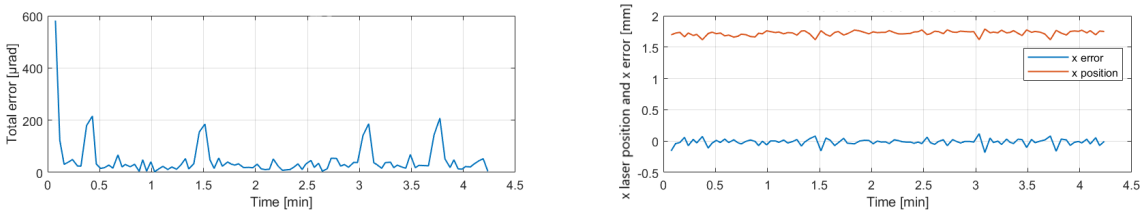

(a) K_p=1, K_i=0.1 and K_d=0.1.

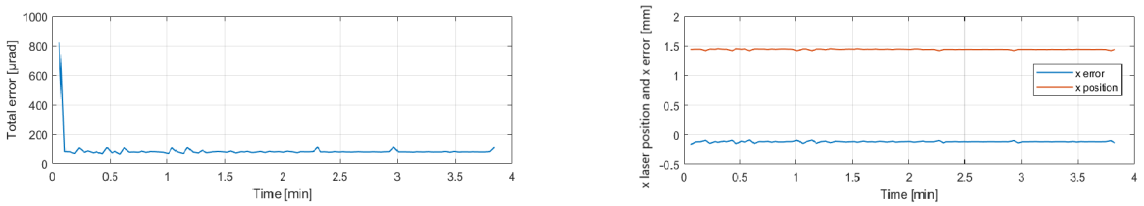

(b) K_p=1, K_i=1 and K_d=0.1.

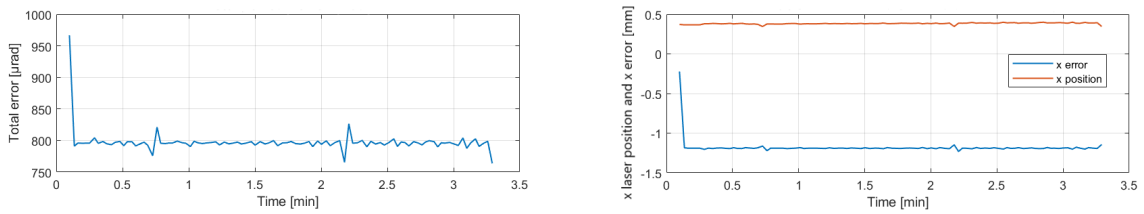

(c) K_p=1, K_i=10 and K_d=0.1.

Figure 4.10: Total error, *x* position of the calibration laser and *x* error over time, when K_i increases.

In (a) the mean total error is 45.7 µrad, and we can see that when there are disturbances, the error comes back to zero, meaning the control system is actuating to correct the error. We can still see that the *x* error oscillates around zero, meaning that in the *x* axis the lasers are aligned. In (b) the mean total

error is 89.1 µrad and it is smoother than (a) over time, but that might have been because there was less turbulence in the simulation. Looking at the *x* position and *x* error, we can see they are also smoother than (a), but the error oscillates around a value minor than zero, like it has an offset. In (c) the mean total error is 797.4 µrad, the x position and *x* error plots are even smoother than (b), and the offset value increases to a mean *x* error of -1.2 mm.

We can conclude that increasing K_i has some pros, such as the laser movement is much more subtle and thus the running time of the 100 cycles decreases. However, there some significant cons like the increase of the mean total error and the error and the offset of the *x* and *y* errors, that indicates there is always an error between the two lasers and thus they are never truly aligned.

Finally, to test the influence the derivative gain, we chose the parameters that led to better results before: K_p=1 and K_i=0.1. Figure 4.11 that the *x* position of the calibration laser and *x* error for K_d=0.1, 1 and 10 is very similar. With the increase of the gain, the *x* position and *x* error get smoother, however, the x error gets a slight offset. The major difference is in the total error plots. The mean total error is 45.7 µrad for (a) 34.1 µrad for (b) and 140.3 µrad for (c).

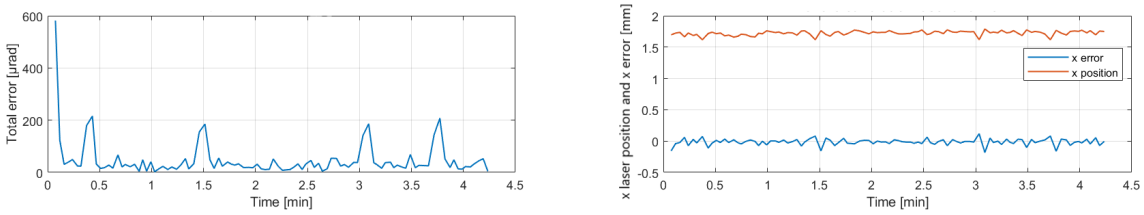

(a) K_p=1, K_i=0.1 and K_d=0.1.

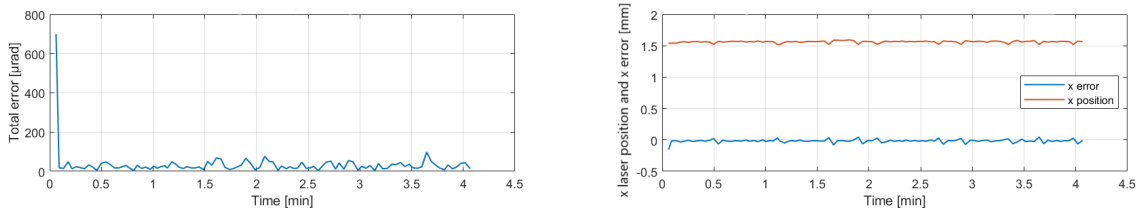

(b) K_p=1, K_i=0.1 and K_d=1.

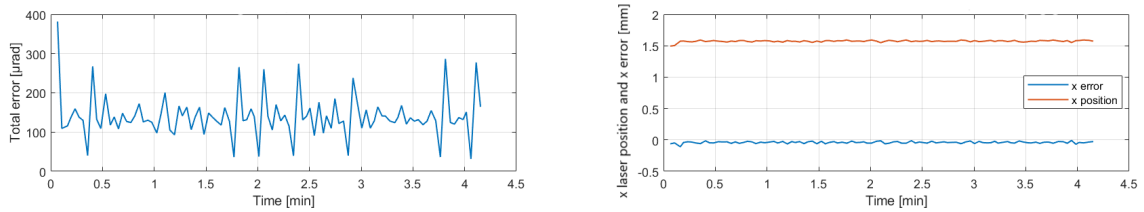

(c) K_p=1, K_i=0.1 and K_d=10

Figure 4.11: Total error, *x* position of the calibration laser and *x* error over time, when K_d increases.

The fact that the derivative terms $\frac{\mathrm{d}e_x(t)}{\mathrm{d}t}$ = 0.0027 and $\frac{\mathrm{d}e_y(t)}{\mathrm{d}t}$ = 0.0198 are so small, makes them to have the least effect in the system response. Even when we raise K_d to 10, the mean total error increases but not as abruptly as when we raise K_p or K_i. Also, it does not influence significantly the time it takes to complete the 100 cycles.

Optimized condition

Analyzing the previous section, we can say that the best gain combinations to get a proper system response are in Figure 4.11 (a) K_p=1, K_i=0.1 and K_d=0.1 and (b) K_p=1, K_i=0.1 and K_d=1. These two options present the lowest mean total errors. In one hand, the *x* error of (a) rounds the zero value, which indicates better alignment. However, it is a bit slower and the movement of the calibration laser is more abrupt. In the other hand, (b) is a bit faster because the calibration laser moves less, but its *x* error has a mild offset, which may indicate the lasers are never completely aligned. To observe this better, we can compare their error scatters in Figure 4.12.

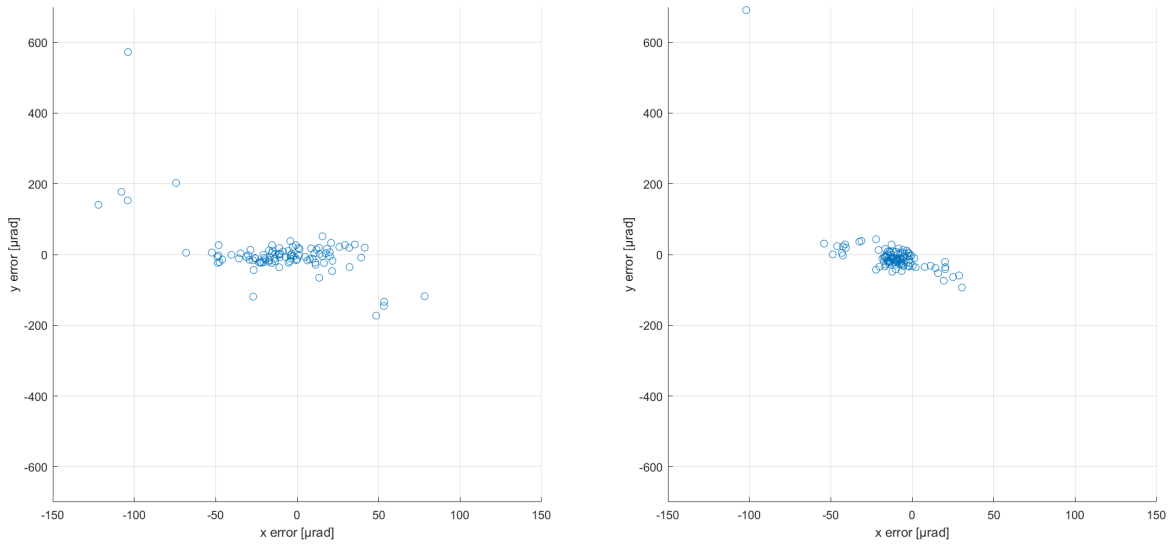

Figure 4.12: Scatter error for (a) K_p=1, K_i=0.1 and K_d=0.1, (b) K_p=1, K_i=0.1 and K_d=1.

It is notorious that 4.12 (b) shows less dispersion, making it a better option, but that does not imply that (a) is not valid. The truth is that both options can be considered adequate, depending on the accuracy requirements of the satellite mission. If the error is less than the accuracy requirement, it means the downlink signal will be received properly. In this case, the error offset present in (b) means the signals are not totally aligned but that does not impede a correct downlink reception.

4.3.2 Downlink data reception

The last objective of the this dissertation is to demonstrate the downlink feasibility for communication. The red laser is modulated, transmitted through the beam splitter, reflected on the mirror and reflected on the same beam splitter towards the telescope. It passes the telescope and makes its way to the ground station, passing the turbulent channel created with the lamps, to simulate the atmosphere. If the fine pointing system is performing well, it will promote the alignment between terminals and it will correct possible disturbances caused by turbulence, allowing the transmitted data to be received at the GS detector. If not, data transmission might not be successful. The ground station detector is connected to an oscilloscope so the received signal is observed in Figure 4.13 in a normal mode and in Figure 4.14

in a high persistence mode, with the intention of emulating an eye diagram analysis.

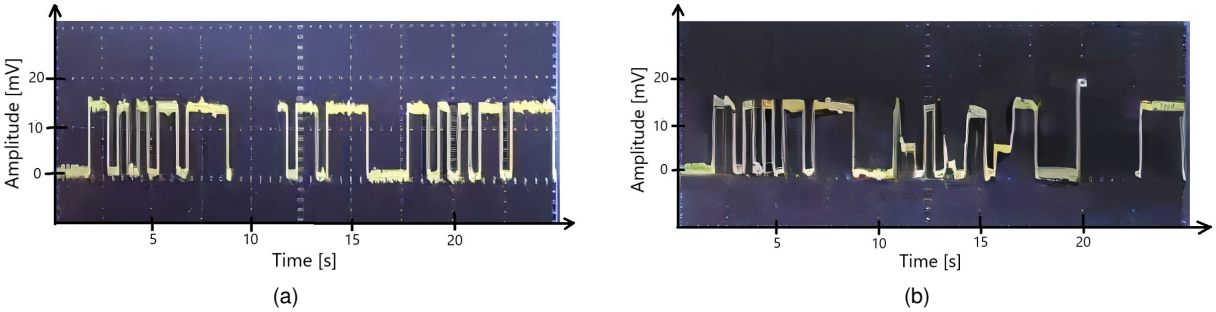

Figure 4.13: Downlink signal received in the ground station detector, observed in a oscilloscope. (a) Closed loop pointing, (b) Without pointing control.

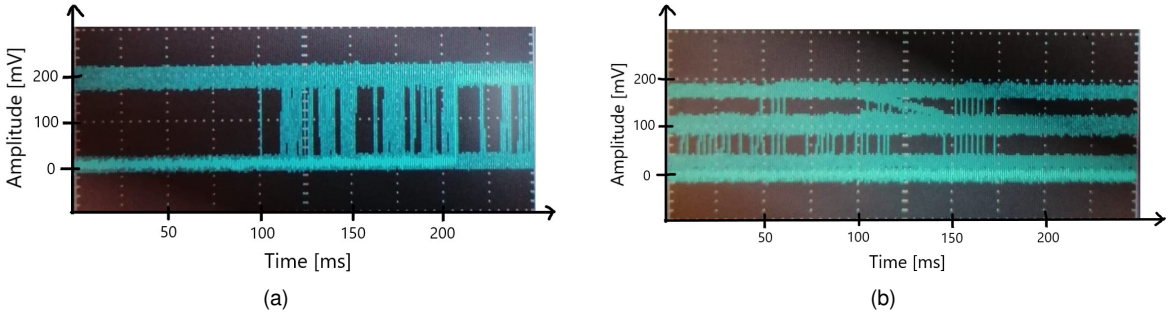

Figure 4.14: Downlink signal received in the ground station detector, observed in a oscilloscope in high persistence mode. (a) Closed loop pointing, (b) Without pointing control.

In the first situation, it was used the PID control with gains K_p = 1, K_i = 0.1 e K_d = 0.1, that has shown to achieve good results in section 4.3. The received downlink signal can be seen in a normal mode in Figure 4.13 (a) and in a infinite persistence mode in Figure 4.14 (a). We observe the two levels of the signal that correspond to levels 1 and 0 of the binary message, and we can see the accumulation of vertical transitions between 1 and 0, leasing to the conclusion that there is good reception of the signal.

In the second situation, Figure 4.13 (b) and 4.14 (b), it was tested the transmission of the downlink signal when the fine pointing system does not use any pointing control (approach used in Figure 4.7). The signal path is the same as in the previous experience, but in this case, the downlink signal is static, so the system does not respond to disturbances. The downlink signal leaves the satellite towards the ground station but when it passes the turbulent channel the beam is disturbed and the system does not respond, compromising the signal reception. The received signal can be seen in a normal mode in Figure 4.13 (b) and in a infinite persistence mode in Figure 4.14 (b). It is noticeable that there are three power levels, instead of two, which does not correspond to the binary message. This happens because when there is a partial misalignment between terminals, only part of the power is received, creating a third level in between 1 and 0. This proves that is essential to use pointing control to guarantee a correct downlink reception.

Chapter 5

Conclusions

5.1 Summary and conclusions

Given the fact that optical communications are being highly explored for satellite systems, this dissertation proposed to implement a closed loop pointing solution that promotes the alignment between an optical ground station and a moving terminal of a satellite.

It was given an overview of optical communications, including modulation schemes used for optical signals, channel noise, the effects of the propagation of an optical signal through the atmosphere such as divergence, attenuation, turbulence and pointing errors, and it was presented a pointing, acquisition and tracking sequence and system.

Three recent pointing systems used for small satellites were studied and from there it was made a proposal for the pointing system to study in this dissertation. The proposed system receives the uplink beacon coming from the ground station and uses a calibration laser assembled on a kinematic mount to track it. This tracking uses closed loop PID control that is described in detail. An image processing algorithm was developed to detect both uplink and calibration spots on the tracking camera and calculate their centroids, and also a control algorithm responsible for tracking the uplink beacon with the calibration beam. Some computational simulation of the closed loop control system was done, concluding that the dynamic elements of the active control have significant impact on the system response and performing control tuning.

Experimentally, it was assembled the proposed pointing system and a block that represents the optical ground station. The uplink beacon was done with a 520 nm laser and the downlink with a 650 nm laser and it was obtained an optimal pointing condition using the PID gain parameters: K_p=K_d=1 and K_i=0.1. Given the assemble, it was concluded that the system can correct errors of a maximum of 3.4 mrad of divergence. For a LEO-to-ground communication at a distance from the Earth of 500 km, this pointing range corresponds to approximately 500 m, which is much greater than the receiver telescope. Finally, the downlink data reception was observed when the optimized pointing control system was used and confirmed a good reception, seeing the transmitted binary message. Assuming the inherency of the optical communication system, namely the low attenuation of the channel conjugated with the tracking

solution here proposed, we consider this as a feasible solution for a long range connection.

5.2 Future Work

For this work to fulfil its objective of controlling the alignment, there are two corrections to apply to the pointing system:

- Develop an algorithm that applies a correction to the calibration laser that instead of overlapping the two beams, sends the calibration laser to the symmetric position of the target, being the center of symmetry the center of the camera. Using a side mirror on the optical design, this is a way to achieve accurate pointing.
- Optimize the integral and derivative terms of the PID controller to try to obtain a better PID response or even explore new types of controllers that might be adequate for this application.

After these improvements are made, future work might be to implement all the control chain algorithms in a microcontroller and test them integrated in a satellite payload. This fine pointing system can be associated to a coarse pointing system to improve the global pointing accuracy and be integrated in a small satellite.

References

[1] A. Trichili, M. A. Cox, B. S. Ooi, and M.-S. Alouini. Roadmap to free space optics. *Journal of the Optical Society of America B*, 37(11):184–201, 2020. doi: 10.1364/JOSAB.399168.

[2] H. Willebrand and B. Ghuman. Fiber optics without fiber. *IEEE Spectrum*, 38:40–45, Sept 2001. doi: 10.1109/6.938713.

[3] V. Chan. Optical space communications. *IEEE Journal of Selected Topics in Quantum Electronics*, 6:959 – 975, Dec 2000. doi: 10.1109/2944.902144.

[4] H. Kaushal and G. Kaddoum. Optical communication in space: Challenges and mitigation techniques. *IEEE Communications Surveys Tutorials*, 19(1):57–96, 2017. doi: 10.1109/COMST.2016.2603518.

[5] O. Cierny. Precision closed-loop laser pointing system for the nanosatellite optical downlink experiment. Master's thesis, Luleå University of Technology, 2017.

[6] D. L. Hutt, K. J. Snell, and P. A. Bélanger. Alexander Graham Bell's PHOTOPHONE. *Opt. Photon. News*, 4(6):20–25, Jun 1993.

[7] J. Hecht. Short history of laser development. *Optical Engineering*, 49(9):1–23, 2010. doi: 10.1117/1.3483597.

[8] G. Nykolak, P. F. Szajowski, J. Jacques, H. M. Presby, J. A. Abate, G. E. Tourgee, and J. Auborn. 4×2.5 Gb/s 4.4 km WDM Free-Space Optical Link at 1550 nm. In *Optical Fiber Communication Conference and the International Conference on Integrated Optics and Optical Fiber Communication*, volume Supplement, pages PD11/1–PD11/3 Suppl. Optical Society of America, 1999. doi: 10.1109/OFC.1999.766044.

[9] E. Ciaramella, Y. Arimoto, G. Contestabile, M. Presi, A. D'Errico, V. Guarino, and M. Matsumoto. 1.28 Terabit/s (32x40 Gbit/s) WDM transmission system for free space optical communications. *IEEE Journal on Selected Areas in Communications*, 27(9):1639–1645, 2009. doi: 10.1109/JSAC.2009.091213.

[10] G. Parca, A. Shahpari, V. Carrozzo, G. M. T. Beleffi, and A. L. J. Teixeira. Optical wireless transmission at 1.6-Tbit/s (16×100 Gbit/s) for next-generation convergent urban infrastructures. *Optical Engineering*, 52(11):1–6, 2013. doi: 10.1117/1.OE.52.11.116102.

[11] DLR Researchers Set World Record in Free-space Optical Communications. URL http://www.parabolicarc.com/2016/11/05/dlr-researchers-set-world-record-freespace-optical-communications/. [Accessed: January 2021].

[12] B. E. Moision, B. I. Erkmen, E. Keyes, T. Belt, O. Bowen, D. Brinkley, P. L. Csonka, M. L. Eglington, A. Kazmierski, N. Kim, J. Moody, T. Tu, and W. Vermeer. Demonstration of free-space optical communication for long-range data links between balloons on Project Loon. In *LASE*, 2017.

[13] L. Li, R. Zhang, Z. Zhao, G. Xie, P. Liao, K. Pang, H. Song, C. Liu, Y. Ren, G. Labroille, P. Jian, D. Starodubov, B. Lynn, R. Bock, M. Tur, and A. E. Willner. High-Capacity Free-Space Optical Communications Between a Ground Transmitter and a Ground Receiver via a UAV Using Multiplexing of Multiple Orbital-Angular-Momentum Beams. *Scientific reports*, 7(1):17427, Dec 2017. doi: 10.1038/s41598-017-17580-y.

[14] S.-K. Liao, W.-Q. Cai, and W.-Y. Liu. Satellite-to-ground quantum key distribution. *Nature*, 549 (7670):43–47, 2017. doi: 10.1038/nature23655.

[15] I. B. Djordjevic. Adaptive Modulation and Coding for Free-Space Optical Channels. *IEEE/OSA Journal of Optical Communications and Networking*, 2(5):221–229, 2010. doi: 10.1364/JOCN.2.000221.

[16] M. Safari and M. Uysal. Do We Really Need OSTBCs for Free-Space Optical Communication with Direct Detection? *IEEE Transactions on Wireless Communications*, 7(11):4445–4448, 2008. doi: 10.1109/T-WC.2008.070637.

[17] T. Tolker-Nielsen and G. Oppenhauser. In-orbit test result of an operational optical intersatellite link between ARTEMIS and SPOT4, SILEX. In *Proceedings of SPIE*, volume 4635, pages 1–15, 2002. doi: 10.1117/12.464105.

[18] A. Katsuyoshi. Overview of the optical inter-orbit communications engineering test satellite (OICETS) project. *Journal of National Institute of Information and Communications Technology*, 59(1/2):5–12, Mar 2012.

[19] M. Handley. Delay is Not an Option: Low Latency Routing in Space. HotNets '18, page 85–91, New York, NY, USA, 2018. Association for Computing Machinery. doi: 10.1145/3286062.3286075.

[20] R. Fields, C. Lunde, R. Wong, J. Wicker, D. Kozlowski, J. Jordan, B. Hansen, G. Muehlnikel, W. Scheel, U. Sterr, R. Kahle, and R. Meyer. NFIRE-to-TerraSAR-X laser communication results: satellite pointing, disturbances, and other attributes consistent with successful performance. In *Proceedings of SPIE*, volume 7330, pages 211–225, 2009. doi: 10.1117/12.820393.

[21] D. N. Amanor, W. W. Edmonson, and F. Afghah. Intersatellite Communication System Based on Visible Light. *IEEE Transactions on Aerospace and Electronic Systems*, 54(6):2888–2899, 2018. doi: 10.1109/TAES.2018.2832938.

[22] L. Wood, W. Ivancic, and K. Dörpelkus. Using Light-Emitting Diodes for intersatellite links. In *2010 IEEE Aerospace Conference*, pages 1–6, 2010. doi: 10.1109/AERO.2010.5446711.

[23] O. M. Kharraz and D. Forsyth. Performance comparisons between PIN and APD photodetectors for use in optical communication systems. *Optik - International Journal for Light and Electron Optics*, 124(13):1493–1498, Jul 2013. doi: 10.1016/j.ijleo.2012.04.008.

[24] P. A. Lightsey. Scintillation in ground-to-space and retroreflected laser beams. *Optical Engineering*, 33(8):2535–2543, 1994. doi: 10.1117/12.173566.

[25] M. Jeganathan, K. E. Wilson, and J. R. Lesh. Preliminary Analysis of Fluctuations in the Received Uplink-Beacon-Power Data Obtained From the GOLD Experiments. *Telecommunications and Data Acquisition Progress Report*, 124:20–32, Oct. 1995.

[26] K. E. Wilson. An Overview of the GOLD Experiment Between the ETS-VI Satellite and the Table Mountain Facility. *Telecommunications and Data Acquisition Progress Report*, 124:8–19, Oct. 1995.

[27] K. E. Wilson. Overview of the Compensated Earth-Moon-Earth Retroreflector Laser Link (CEMERLL) experiment. In G. S. Mecherle, editor, *Free-Space Laser Communication Technologies VI*, volume 2123, pages 66–74. International Society for Optics and Photonics, SPIE, 1994. doi: 10.1117/12.184685.

[28] D. R. Kolev and M. Toyoshima. Received-Power Fluctuation Analysis for LEO Satellite-to-Ground Laser Links. *Journal of Lightwave Technology*, 35(1):103–112, 2017. doi: 10.1109/JLT.2016.2627038.

[29] V. W. S. Chan. Optical satellite networks. *Journal of Lightwave Technology*, 21(11):2811–2827, 2003. doi: 10.1109/JLT.2003.819534.

[30] G. A. Mahdiraji and E. Zahedi. Comparison of Selected Digital Modulation Schemes (OOK, PPM and DPIM) for Wireless Optical Communications. pages 5–10, Jul 2006. doi: 10.1109/SCORED.2006.4339297.

[31] R. Mesleh, H. Elgala, and H. Haas. On the Performance of Different OFDM Based Optical Wireless Communication Systems. *Journal of Optical Communications and Networking*, 3(8):620–628, 2011. doi: 10.1364/JOCN.3.000620.

[32] Z. Ghassemlooy, W. Popoola, and S. Rajbhandari. *Optical Wireless Communications System and Channel Modelling with MATLAB®*. CRC Press, 2012.

[33] ITU-R. Propagation Data Required for the Design of Earth- Space Systems Operating Between 20 THz and 375 THz. Recommendation P.1621, 2003.

[34] I. I. Kim, B. McArthur, and E. J. Korevaar. Comparison of laser beam propagation at 785 nm and 1550 nm in fog and haze for optical wireless communications. In *Proceedings SPIE*, volume 4214, pages 26–37, 2001. doi: 10.1117/12.417512.

[35] A. Ghassemi, A. Abedi, and F. Ghasemi. *Propagation Engineering in Wireless Communications*. Springer, 2012.

[36] M. A. Esmail, H. Fathallah, and M. Alouini. An Experimental Study of FSO Link Performance in Desert Environment. *IEEE Communications Letters*, 20(9):1888–1891, 2016. doi: 10.1109/LCOMM.2016.2586043.

[37] K. Kazaura, K. Omae, T. Suzuki, M. Matsumoto, E. Mutafungwa, T. Korhonen, T. Murakami, K. Takahashi, H. Matsumoto, K. Wakamori, and Y. Arimoto. Enhancing performance of next generation FSO communication systems using soft computing-based predictions. *Optics express*, 14:4958–68, Jul 2006. doi: 10.1364/OE.14.004958.

[38] S. Bloom, E. Korevaar, J. Schuster, and H. Willebrand. Understanding the performance of free-space optics [Invited]. *Journal of Optical Networking*, 2(6):178–200, Jun 2003. doi: 10.1364/JON.2.000178.

[39] M. M. Abadi, M. A. Cox, R. E. Alsaigh, S. Viola, A. Forbes, and M. P. J. Lavery. A space division multiplexed free-space-optical communication system that can auto-locate and fully self align with a remote transceiver. *Scientific Reports*, 9(1):19687, 2019. 10.1038/s41598-019-55670-1.

[40] R. Kingsbury, K. Riesing, and K. Cahoy. Design of a free-space optical communication module for small satellites. `https://digitalcommons.usu.edu/smallsat/2014/AdvTechComm/6/`, 2014. [Accessed: October 2021].

[41] K. Riesing. Development of a pointing, acquisition, and tracking system for a nanosatellite laser communications module. Master's thesis, Massachusetts Institute of Technology, 2015.

[42] Q. Li, H. Guo, S. Xu, Y. Xu, Q. Wang, D. He, Z. Peng, and Y. Huang. TRC-Based High-Precision Spot Position Detection in Inter-Satellite Laser Communication. *Sensors*, 20:5649, Oct 2020. doi: 10.3390/s20195649.

[43] Q. Li, S. Xu, J. Yu, L. Yan, and Y. Huang. An Improved Method for the Position Detection of a Quadrant Detector for Free Space Optical Communication. *Sensors*, 19(1), 2019. doi: 10.3390/s19010175.

[44] W. Xuan, S. Xiuqin, G. Liu, J. Huang, K. Wang, and W. Zhu. A Method for Improving the Detection Accuracy of the Spot Position of the Four-Quadrant Detector in a Free Space Optical Communication System. *Sensors*, 20, Dec 2020. doi: 10.3390/s20247164.

[45] K. Cahoy, P. Grenfell, A. Crews, M. Long, P. Serra, A. Nguyen, R. Fitzgerald, C. Haughwout, R. Diez, A. Aguilar, J. Conklin, C. Payne, J. Kusters, C. Sackier, M. LaRocca, and L. Yenchesky. The CubeSat Laser Infrared CrosslinK Mission (CLICK). In Z. Sodnik, N. Karafolas, and B. Cugny, editors, *International Conference on Space Optics — ICSO 2018*, volume 11180, pages 358–369. International Society for Optics and Photonics, SPIE, 2019. doi: 10.1117/12.2535953.

[46] L. Zhang, J. Dai, C. Li, J. Wu, J. Jia, and J. Wang. Design and in-orbit test of a high accuracy pointing method in satellite-to-ground quantum communication. *Opt. Express*, 28(6):8291–8307, Mar 2020. doi: 10.1364/OE.387011.

[47] Wikipedia. PID controller - Wikipedia, the free encyclopedia. `http://en.wikipedia.org/w/index.php?title=PID%20controller&oldid=1052917271`, 2021. [Accessed: September 2021].